



1

1 **Assessment of the Finite VolumE Sea Ice Ocean Model** 2 **(FESOM2.0), Part II: Partial bottom cells, embedded sea ice and** 3 **vertical mixing library CVMIX**

4

5 Patrick Scholz¹, Dmitry Sidorenko¹, Sergey Danilov^{1,2}, Qiang Wang¹, Nikolay Koldunov¹, Dmitry
6 Sein^{1,4}, Thomas Jung^{1,3}

7

8 ¹ Alfred Wegener Institute Helmholtz Center for Polar and Marine Research (AWI), Bremerhaven, Germany

9 ² Jacobs University Bremen, Department of Mathematics & Logistics, Bremen, Germany

10 ³ University of Bremen, Department of Physics and Electrical Engineering, Bremen, Germany

11 ⁴ Shirshov Institute of Oceanology, Russian Academy of Science, 36 Nahimovskiy Prospect, Moscow, Russia 117997

12

13 Correspondence to: Patrick Scholz (Patrick.Scholz@awi.de)

14

15 **Abstract**

16 The second part of the assessment and evaluation of the unstructured-mesh Finite-volumE Sea ice-Ocean
17 Model version 2.0 (FESOM2.0) is presented. It focuses on the performance of partial cells, embedded sea ice
18 and on the effect of mixing parameterisations available through the CVMIX package.

19 It is shown that partial cells and embedded sea ice lead to significant improvements in the representation of
20 the Gulf Stream and North Atlantic Current as well as the circulation of the Arctic Ocean. In addition to the
21 already existing Pacanowski and Phillander (fesom_PP) and K-profile (fesom_KPP) parameterisations for
22 vertical mixing in FESOM2.0, we document the impact of several mixing parameterisations from the
23 Community Vertical Mixing (CVMIX) project library. Among them are the CVMIX versions of Pacanowski
24 and Phillander (cvmix_PP) and K-profile (cvmix_KPP) parameterisations, the tidal mixing parameterisation
25 (cvmix_TIDAL), a vertical mixing parameterisation based on turbulent kinetic energy (cvmix_TKE) as well
26 as a combination of cvmix_TKE and the recent scheme for the computation of the Internal Wave
27 Dissipation, Energy and Mixing (IDEMIX). The IDEMIX parameterises the redistribution of internal wave
28 energy through wave propagation, nonlinear interactions and the associated imprint on the vertical
29 background diffusivity. Further, the benefit from using a parameterisation of sea ice melt season mixing in
30 the surface layer (MOMIX) for reducing Southern Ocean hydrographic biases in FESOM2.0 is presented.
31 We document the implementation of different model components and illustrate their behaviour. This paper
32 serves primarily as a reference for FESOM users but is also useful to the broader modelling community.

33 **1 Introduction**

34 Global unstructured-mesh ocean models start to be widely used in climate studies, including the recent
35 CMIP6 simulations (Semmler et al., 2020), although structured-mesh ocean general circulation models are
36 still more mature in terms of features, functionality and complexity due to their long development history.
37 However, step by step, also the unstructured-mesh ocean models acquire new features and catch up in their

2

1



3

38 functionality. This paper continues the work by Scholz et al. (2019) in documenting the features available in
39 Finite volumE Sea ice Ocean Model version 2.0 (FESOM2.0, Danilov et al., 2017). It focuses on two
40 aspects. The first one is about partial bottom cells and embedded sea ice, both of which essentially rely on
41 the Arbitrary Lagrangian Eulerian (ALE) vertical coordinates used in FESOM2.0. The second one deals with
42 mixing parameterizations enabled through the use of Community Ocean Vertical Mixing (CVMIX, Griffis et
43 al. 2015, Van Roekel et al. 2018) package.

44 Partial bottom cells were first introduced for a finite volume model by Adcroft et al., (1997), as an attempt to
45 improve the representation of the bottom topography in general ocean circulation models. Adcroft et al.,
46 (1997) introduces partial bottom cells as a compromise solution between the less accurate but
47 computationally efficient full cell approach and the very accurate but computationally expensive shaved cell
48 approach. Partial bottom cells are implemented in FESOM2.0 by using the vertical ALE approach of
49 FESOM2.0 numerical core documented in Danilov et al. 2017.

50 Another feature made available through using ALE in FESOM2.0 is related to the sea ice-ocean interaction.
51 Naturally, sea ice, more precisely the loading of sea ice, contributes to the ocean pressure. However in many
52 ocean models, especially in the absence of surface mass fluxes or on fixed vertical grids, the loading is
53 omitted and sea ice is treated as “levitating”. The option to consider sea ice loading is now implemented into
54 FESOM2.0, which is called “embedded” sea ice and was first introduced by Campin et al. (2008). They state
55 that the advection of sea ice in combination with the coupling of “embedded” sea ice through ice loading can
56 be an important source of ocean variability especially in the vicinity of ice edges (Campin et al. 2008). The
57 implementation of embedded sea ice relies on the zstar vertical-coordinate option in FESOM2 and also on
58 the fact that the sea ice component is called on each time step of the ocean model.

59 Diapycnal mixing in the ocean is an essential process that acts on the ocean stratification and the distribution
60 of heat, salt as well as passive tracers like nutrients, biological agents or CO₂. Various processes contributing
61 to diapycnal mixing can act with different magnitudes over a wide range of horizontal and vertical scales,
62 from several kilometers down to centimeters (Robertson and Dong, 2019). Due to the finite discretisation
63 scale in all ocean models, the mixing processes can not be resolved and thus must be parameterized. The
64 parameterisations of diapycnal mixing can be done in a variety of ways with different complexity, such as
65 boundary layer schemes like the K-profile parameterisation of Large et al. (1994) or turbulent closure
66 schemes like the one of Gaspar et al. 1990 and many others. A great innovation in the ocean modelling
67 community is the development of software packages that contain a variety of vertical mixing
68 parameterisations in a format that makes it easy to integrate them into existing model code (Fox Kemper et
69 al. 2019). One of these software packages is the Community Ocean Vertical Mixing package (CVMIX,
70 Griffis et al. 2015, Van Roekel et al. 2018), which now also was integrated into FESOM2.0. CVMIX is
71 tailored to be used in state of the art climate models to produce vertical profiles of diffusivity and viscosity
72 (Fox Kemper et al. 2019), providing a comparable mixing implementation over a wide spread of different
73 ocean models such as MOM6, POP, MPAS and ICON. Such effort makes it easier to compare these models

4

2



5

74 to each other. From the CVMIX package we implemented the Pacanowski and Philander 1981, the K-profile
75 parameterization of Large et al. 1994 and the tidal mixing parameterisation of Simmons et al. 2004. Further,
76 the infrastructure of the CVMIX library has been used to implement the turbulent kinetic energy (TKE)
77 scheme of Gaspar et al. (1990) and the scheme for Internal Wave Dissipation and Mixing (IDEMIX) of
78 Olbers and Eden (2013) in the same way as it is done in Gutjahr et al. (2020). It should be mentioned that
79 neither TKE nor IDEMIX is yet part of the official CVMIX package but will hopefully be added to the
80 package in the future.

81 Beside the prime vertical mixing schemes, like the K-profile scheme, the Pacanowski and Phillander scheme
82 and others that have the purpose to deliver a usable mixing parameterisation for the entire ocean, and vertical
83 mixing schemes like the tidal mixing scheme of Simmons et al. 2004 or IDEMIX that are used to
84 parametrize internal wave processes which then result in a heterogeneous background diffusivity, there are
85 also mixing parameterizations that aim at resolving regional processes. One of them was proposed by
86 Timmerman and Beckmann (2004). It parameterises the wind driven mixing in the Southern Ocean
87 especially when there is insufficient mixing during the melt seasons when other mixing schemes are used. It
88 is used in FESOM2.0 to improve the otherwise too low stratification in the Southern Ocean and Weddell
89 Sea.

90 The intention of this paper is to document the performance of the newly implemented features -- partial
91 bottom cells, “embedded” sea ice, the vertical mixing parameterisations that come with the implementation
92 of CMVIX and the local mixing parameterization of Timmerman and Beckmann (2004), based on comparing
93 the associated hydrographic biases, changes in vertical convection and differences in Meridional Overturning
94 Circulation, using a relatively coarse reference mesh.

95 The paper is structured as follows. First in Section 2 we describe the mesh configuration and model setup
96 used in the simulations. The description and analysis of partial bottom cells, “embedded” sea ice and vertical
97 mixing schemes is done in Section 3. A discussion and conclusion is given in Section 4.

98 **2 Model configurations**

99 We use here the FESOM2.0 coarse mesh configuration core2, which is the same mesh as in part 1. It consists
100 of ~0.13M surface vertices, with a nominal resolution of 1° in the bulk of the ocean, ~25km north of 50°N,
101 1/3° in the equatorial belt and slightly enhanced resolution in the coastal regions. In the vertical, 48 unevenly
102 distributed layers are used, with a vertical grid spacing stepwise increasing from 5m at the surface to 250 m
103 towards the bottom.

104 All model simulations are initialised from the Polar Science Center Hydrographic winter Climatology
105 (PHC3.0, updated from Steele et al., 2001) and forced by the CORE interannually varying atmospheric
106 forcing fields (Large and Yeager, 2009) for the period 1948-2009. For each simulation a spin-up over three
107 full CORE cycles was applied, where each subsequent cycle was initialised with the final results from the
108 preceding cycle. All modelled data shown in this work are averaged over the period 1989-2009.

6

3



7

109

110 All model simulations except the one with the Turbulent-Kinetic-Energy (TKE) closure mixing of Gaspar et
111 al., 1990, use a non-constant latitude-dependent vertical background diffusivity with values between 10-4
112 m²/s and 10-6 m²/s, as described in Scholz et al., 2019. Further, all simulations use the Monin-Obukhov
113 length dependent vertical mixing parameterization of Timmermann and Beckmann, 2004 in the surface
114 boundary layer south of -50°S. The effects of this parameterisation on the simulated ocean state in
115 FESOM2.0 is described in section 3.4. The horizontal viscosity is computed via a modified harmonic Leith
116 approach (Fox-Kemper and Menemenlis, 2008) plus a biharmonic background viscosity (0.01 m²/s) . For
117 coarse-mesh setups, like the one used here, FESOM2.0 uses the Gent-McWilliams (GM) parameterisation
118 for eddy stirring (Gent et al., 1995; Gent and McWilliams, 1990) and we follow the implementation after
119 Ferrari et al., 2010. The isoneutral tracer diffusion (Redi, 1982) coefficient equals to that of GM, same as in
120 Scholz et al. (2019) and in previous FESOM versions (Wang et al. 2014). GM and Redi are scaled with
121 horizontal resolution with a maximum value of 3000 m²/s at 100 km horizontal resolution and change
122 linearly to zero between a resolution of 40 km and 30 km. In the vertical, they are scaled according to Ferrari
123 et al., 2010 and Wang et al., 2014. The simulations use as default the K-profile parameterisation for vertical
124 mixing (KPP, Large et al., 1994), a linear free surface (Scholz et al., 2019), levitating sea ice and a full
125 bottom cell approaches, unless otherwise stated.

126 **3 FESOM2.0 model components and evaluation**

127 **3.1 Partial bottom cells**

128 The concept of partial cells, as an attempt to improve the bottom representation in general ocean circulation
129 models, which was first introduced for the finite volume approach by Adcroft et al., (1997). Although an
130 early version of partial cells was developed by Cox, (1977), and used by Semtner and Mintz, (1977) and
131 Maier-Reimer et al., (1993), it has never got officially released (Griffies et al., 2000). Adcroft et al.
132 (1997) presented three different cases. The first one is the conventional full cell approach, where the depth of
133 the ocean bottom is approximated with the nearest standard depth level of the vertical model discretization.
134 The second one is the partial cell approach in which the bottom level can take any intermediate depth within
135 the cell, thus capturing water columns more accurately. In these two cases, the bottom features a “stepped”
136 topography and the jump of the steps is smaller for the partial cell approach (Adcroft et al., 1997). The third
137 case introduced by Adcroft et al., (1997) is a shaved cell approach, which assumes a constant slope within
138 each bottom cell and gives the best approximation for a continuous bottom topography. Adcroft et al.
139 (1997) showed that the shaved cell approach gives the most accurate results, but induces a significant
140 increase in computational demand, whereas the partial cell approach is a good compromise between the low
141 computational demand of the full cell approach and the increased accuracy of the shaved cell approach.
142 Hence, most ocean models (e.g. NEMO, MOM6, MPAS, POP) including FESOM2.0 went in favor of the



9

143 partial cell approach.

144 For the implementation of partial cells in FESOM2.0 we follow the work of Pacanowski and Gnanadesikan,
145 (1998), which implemented partial cells for the B-grid discretization in MOM2 with efforts to minimize
146 pressure gradient errors and spurious diapycnal mixing. They addressed that calculating horizontal pressure
147 gradients needs some special attention for partial cells since not all grid points within the bottom layer are at
148 the same depth. In FESOM2.0, we compute pressure gradient force based on the density Jacobian approach
149 as used by Shchepetkin, (2003) and not the pressure Jacobian approach proposed by Pacanowski and
150 Gnanadesikan, (1998). The density Jacobian approach is less prone to pressure-gradient error than using
151 pressure Jacobian, and therefore the model is more stable. Furthermore, we limited the thickness of the
152 partial bottom cell to be at least half of the full cell layer thickness to reduce the possibility of violating the
153 vertical Courant–Friedrichs–Lewy (CFL) criterion.

154 Using a B-grid like discretisation, where the scalars are located at vertices of a triangular mesh while the
155 velocities are located at the centroids of the triangular elements, makes it necessary to define the partial cells
156 at both locations. First, the partial bottom depth is defined at the centroids of the triangular elements based
157 on the real bottom topography considering the aforementioned limitation. Then, the vertice partial bottom
158 depth is derived from the deepest partial bottom of the surrounding triangular elements.

159 In order to demonstrate the effect of the partial cells on the simulated ocean state we performed two model
160 simulations using the full cell and partial cell approaches, respectively. We investigate, first, the temperature
161 biases of the full cell approach with respect to the data of the World Ocean Atlas 2018 (WOA18, Locarnini
162 et al., 2018; Zweng et al., 2018, in the left column of Fig. 1) and, second, the temperature differences
163 between partial cell and full cell (partial-full) averaged over five different depth ranges 0-250m, 250-500m,
164 500-1000m, 1000-2000m and 2000-4000m (in the right column of Fig. 1).

165 The full cell setup (Fig. 1, left) shows positive climatological temperature bias in the northern and southern
166 Pacific, the Atlantic equatorial ocean as well as in the central Indian Ocean through the depth ranges of 0-
167 250m, 250-500m and 500-1000m. In the same depth ranges there are also negative biases in the North
168 Atlantic (NA) subtropical gyre and in the equatorial and southern subtropical Pacific. The depth ranges of
169 250-500m and 500-1000m indicate cold biases in the Southern Ocean (SO) and around the coast of
170 Antarctica. The deeper depth ranges (1000-2000m and 2000-4000m.) indicate small negative temperature
171 biases in most of the world oceans, except for the Atlantic and Arctic Ocean (AO), which possess a small
172 warming bias in the depth ranges. The Arctic warming anomaly at these depths originates largely from a
173 vertically too much extended Atlantic water inflow branch (not shown), which is a typical feature of coarse
174 resolution models (e.g., Ilicak2016).

175 Using partial cells (Fig. 1, right) leads to profound changes especially at the position of zonal fronts in the
176 North and South Atlantic. In the depth ranges of 0-250 m, 250-500 m and 500-1000 m in the NA, partial
177 cells lead to a cooling in the Labrador Sea (LS) and Irminger Sea (IS) as well as along the path of the Gulf
178 Stream (GS) and North Atlantic Current (NAC), except for the area around -30°W, 50°N which is



11

179 characterised by warming. In the upper South Atlantic (SA), partial cells lead to a northward shift of Brazil–
180 Malvinas Confluence Zone expressed by a dipole of warmer South Atlantic Current (SAC) and cooler
181 Antarctic Circumpolar Current (ACC). Further, partial cells lead to a predominant cooling in the SO Atlantic
182 sector and parts of the Indian Ocean sector, while the Pacific sector of the SO and most of the Antarctic
183 coastal areas are dominated mostly by warming anomalies. The Arctic Ocean features a slight warming
184 anomaly at all depths, except for the surface, when using partial cells instead of full cells.

185 Fig. 2 shows the same as Fig. 1 but for salinity. Here, with respect to WOA18, the full cell run indicates a
186 generally fresher AO for the surface- and the 250-500 m depth range. Further negative salinity biases can be
187 found within the upper three depth ranges in the equatorial Pacific, north and south subtropical Atlantic, at
188 the position of the Atlantic northwest corner, northern IO as well as parts of the SO. Strong positive salinity
189 biases with full cells can be found in the surface depth range of the North Pacific and in the Chukchi- and
190 Beaufort Sea. Further positive salinity biases in the 250-500 m and 500-1000 m depth ranges are found along
191 the pathway of the Gulf Stream as well as in the equatorial Atlantic and central IO. The deep depth range of
192 1000-2000m has positive salinity anomalies in the Northern and Southern Atlantic and negative salinity
193 biases in the Mediterranean outflow branch and IO.

194 Using partial cells leads to an increase in salinity throughout all depth ranges of the AO relative to using full
195 cells. Further, a salinity increase at the position of the “cold blob”, in the GIN sea, in the eastern South
196 Atlantic and parts of the SO can be observed within the upper three depth ranges. Compared to full cells,
197 using partial cells reduces salinity along the pathway of the GS, the Antarctic Circumpolar Current (ACC) in
198 the South Atlantic and along the coast of Antarctica.

199 The differences in the horizontal velocity speed between partial and full cells (Fig. 3), for the depth ranges of
200 0-250 m, 250-500 m, 500-1000 m, 1000-2000 m, 2000-4000 m and at the bottom, reveal that with partial
201 cells the velocity in the East Greenland Current (EGC), West Greenland Current (WGC) and Labrador
202 Current (LC) are stronger by up to 0.02 m/s through all depth ranges presented here. The upper differences
203 reveal that partial cells lead to a weakening and a slight southwards shift of the NAC between -45°W and -
204 30°W, and a more pronounced tendency towards a northwest bend of the NAC between -30°W and -15°W,
205 which is nevertheless still too far eastward. By using partial cells the pathway of the Irminger Current (IC)
206 moves closer to the continental slope.

207 In terms of absolute and anomalous northern and southern hemispheric maximum mixed layer depth (MLD),
208 using partial cells leads to a slight MLD decrease in the southern LS, IS and northern Greenland-Iceland-
209 Norwegian (GIN) Seas, and a slight MLD increase along the pathway of the IC and in the southern and
210 central GIN Seas (Fig. 4c). In the southern hemisphere, partial cells have a more pronounced effect, leading
211 to a significant, up to 1000 m, decrease in MLD in the central Weddell Sea (WS) and a minor increase in
212 MLD of around 300 m along the eastern continental slope of the Antarctic Peninsula.

213 The differences between using full cells and partial cells in Global-, Atlantic- and Indo-Pacific Overturning
214 Circulation (Fig. 5) are rather small with magnitudes of less than 1Sv. Both cases feature an upper AMOC



13

215 circulation cell of ~ 16 Sv and an Antarctic Bottom Water (AABW) cell with strength between -1 Sv and -2
216 Sv. One can summarize that partial cells lead to a clear improvement of the circulation pattern, especially
217 regarding the branch of the Gulf Stream and NAC even in rather coarse resolved configurations.

218 **3.2 Embedded sea ice**

219 As described in Scholz et al. (2019), FESOM2.0 supports the full free surface formulation with two possible
220 options, zlevel and zstar (Adcroft and Campin, 2004). Both options allow for surface freshwater exchanges
221 which can modify the thickness of the surface layer and thus decrease or increase salinity in the surface
222 layer. This avoids the need of virtual salinity fluxes, which are required in the linear free surface (linfs)
223 approach when the layer thicknesses are kept fixed. Using virtual salinity fluxes has the potential to affect
224 the model integrity on long timescales and change local salinities with certain biases (Scholz et al., 2019).

225 In reality part of sea ice is embedded in the ocean with impact on the ocean pressure below. In the model,
226 when the sea ice loading is omitted, the “levitating” sea ice (Campin et al., 2008) does not impose pressure
227 on the ocean. This is the default case in the case of linfs but also applicable to zlevel and zstar. The other
228 case when ice-loading is considered has “embedded” sea ice (Rousset et al., 2015), which depresses the sea
229 surface according to its mass. Since it affects the layer thicknesses, this case is only available for the full free
230 surface cases of zlevel and zstar. Although freezing and melting have no direct effect on the oceanic
231 pressure, the divergence of the ice transport does modify the ice-loading fields and influences the hydrostatic
232 pressure (Campin et al., 2008). As mentioned by Campin et al., 2008, this effect could be compensated by
233 the divergence of the oceanic transport in the special case where sea ice and ocean velocities match, but in
234 reality sea ice and ocean velocities are rarely identical especially in the presence of high frequency wind
235 forcing. Therefore, sea ice dynamics in combination with the ice-loading coupling can be a source of oceanic
236 variability especially near the ice-edge where ice divergence/convergence is large (Campin et al., 2008).
237 However, using embedded sea ice harbours the risk that the amount of sea ice loading due to excessive
238 accumulation and the resulting depression in the surface elevation may result in a depletion of the surface
239 layer thickness, when the zlevel option is used, where only the surface layer is allowed to change. To avoid
240 this issue, we limit in FESOM2.0 the maximum ice loading to a sea ice height of 5m when the zlevel option
241 is used. In case of using zstar, the problem is less severe, since here the change in elevation is distributed
242 over all vertical layers, except for the bottom one. This makes zstar to be the recommended option when
243 using embedded sea ice, as also stated by Campin et al., 2008.

244 To show the effect of embedded sea ice on the simulated ocean state, two simulations were carried out using
245 the zstar option of FESOM2.0, one with levitating (omitting the effect of sea ice loading on ocean pressure)
246 the other with embedded sea ice (including the effect of sea ice loading on ocean pressure).

247 Fig. 6 shows the sea ice concentration (SIC) for March and September in the levitating sea ice case and the
248 difference between the embedded and levitating sea ice cases. Superimposed are the simulated (solid) and
249 observed (dashed, Cavalieri et al., 1996) contour line of the 15% sea ice extent. The northern hemispheric



15

250 March sea ice edge (Fig. 6a) shows a good agreement with observational data for the LS, IS and Bering Sea
251 but reveals a too far southwards extension in the Greenland Sea and Barents Sea. The simulated northern
252 hemispheric September sea ice extent (Fig. 6b) is larger than the observations. The southern hemispheric
253 March sea ice extent is underestimated in the simulation, while the simulated southern hemispheric
254 September sea ice extent is in good agreement with the observation.

255 Using the embedded sea ice leads to an increase in the SIC in the Greenland Sea by around 6% in March. In
256 September, embedded sea ice leads to positive SIC anomalies in the eastern- and negative anomalies in the
257 western AO. In the southern hemisphere, embedded sea ice leads to a heterogeneous pattern of small positive
258 and negative changes along the sea ice edge.

259 Regarding the changes in the ocean, Fig. 7 shows the temperature (left column) and salinity (right column)
260 differences between the embedded and levitating (embedded minus levitating) sea ice cases averaged over
261 the depth ranges 0-250 m, 250-500 m, 500-1000 m, 1000-2000 m and 2000-4000 m. The temperature and
262 salinity differences reveal that a significant warming of up to 0.5°C and a salinification of up to 0.10 psu
263 occurs in almost the entire AO due to embedded sea ice, except in a thin stripe along the eastern continental
264 shelf of the AO that shows negative anomalies in the depth ranges of 0-250 m, 250-500 m and 500-1000 m.
265 The changes in temperature and salinity can be explained by the changes in ocean currents. Figure 8 depicts
266 the speed of the horizontal currents in levitating (1st column) and embedded (2nd column) sea ice cases as
267 well as their difference (3rd column). Using embedded sea ice leads to an increase in the speed along the
268 entire boundary current of the Eurasian Basin and along the Lomonosov Ridge, that can be found in all three
269 presented depth ranges. The increase in the velocity of the boundary currents, caused by using embedded sea
270 ice, leads to an enhanced heat and salt transport in the Atlantic water layer originating from the Fram Strait,
271 which results in a warmer and more saline intermediate depth in the Arctic Ocean. The increase in
272 temperature and salinity, especially in the surface layers of the AO using embedded sea ice reduces existing
273 local biases (see Fig. 1 and Fig. 2) that occur when using levitating sea ice. On the whole it can be stated that
274 using embedded sea ice instead of levitating sea ice has some significant effect on the ocean dynamics of the
275 AO, but no effect in the Southern Ocean or Antarctic marginal seas.

276 3.3 Implementation and evaluation of vertical mixing schemes

277 Besides the already existing Pacanowski and Philander (fesom_PP, Pacanowski and Philander, 1981) and
278 MOM5 K-profile (fesom_KPP, Large et al., 1994) vertical mixing parameterizations in FESOM2.0 that were
279 based on the implementation in the predecessor version FESOM1.4, the vertical mixing parameterizations of
280 the Community Vertical Mixing (CVMIX, Griffies et al., 2015) project have been now added as well. This
281 includes the CVMIX vertical mixing of: Pacanowski and Philander (cvmix_PP), the MOM6 K-profile
282 (cvmix_KPP) parameterization, the tidal mixing parameterization of Simmons et al., (2004) (cvmix_TIDAL)
283 and the turbulent kinetic energy (cvmix_TKE) mixing of (Gaspar et al., 1990) in combination with the
284 Internal Wave Dissipation, Energy and Mixing (IDEMIX) parameterization (Olbers and Eden, 2013 and



17

285 Eden and Olbers, 2014) . Although `cvmix_TKE` and `IDEMIX` are not yet a part of the `CVMIX` project, they
286 use its libraries in the background and will join the project in the future. `CVMIX` is used by a variety of
287 models, such as `MOM6`, `POP`, `MPAS` or `ICON` and provides an opportunity of a cross model-spanning
288 vertical mixing implementation that allows for an enhanced cross-model intercomparison.

289

290 **3.3.1 Comparison of `cvmix_KPP`, `cvmix_PP` with previous `fesom_KPP` and `fesom_PP`** 291 **implementation**

292 In `FESOM2.0` we implemented `cvmix_PP` and `cvmix_KPP` in addition to its previous implementations
293 `fesom_PP` and `fesom_KPP` that were adopted from `FESOM1.4`. The difference between `cvmix_PP` and
294 `fesom_PP` lies in the background coefficient for viscosity which is considered in `cvmix_PP` but not in
295 `fesom_PP` when computing the diffusivity, following the experience with `FESOM1.4` which did not need to
296 be more diffusive. The difference between `cvmix_KPP` and `fesom_KPP` lies mainly in the treatment of the
297 squared velocity shear and buoyancy difference with respect to the surface. In `cvmix_KPP` the surface
298 quantities are computed by averaging over the Monin-Obukov surface layer (Griffies et al. 2015) while in
299 `fesom_KPP` the surface values are linked to the first layer in the model.

300 Suppl. 2 displays the temperature (1st and 2nd column) and salinity (3rd and 4th column) biases of `fesom_KPP`
301 with respect to `WOA18` (1st and 3rd column) as well as the difference between `fesom_PP` and `fesom_KPP` (2nd
302 and 4th column). In the surface depth range the climatological temperature and salinity biases of `fesom_KPP`
303 with respect to `WOA18` are largely negative in the tropical and subtropical Pacific, North and South Atlantic
304 as well as AO, and positive in tropical Atlantic and Indian Ocean, Southern Ocean, Labrador Sea, GIN Seas
305 and the marginal seas of the North Pacific. The subsurface depth ranges of 250-500 m and 500-1000 m are
306 dominated by largely positive temperature biases, except for the Southern Ocean, the pathway of the GS and
307 NAC and the northern Indian Ocean. The salinity biases in the 250-500 m and 500-1000 m depth range
308 preserve largely the pattern from the surface layer except for an increasing and expanding positive salinity
309 bias in the tropical Atlantic, reduced positive salinity biases in the Indian Ocean and northern Pacific as well
310 as reduced negative biases in the Arctic Ocean. The 1000-2000 m depth range features small warm biases in
311 the AO and GIN seas, positive temperature and salinity biases in the LS and the South Atlantic, negative
312 temperature and salinity biases in the eastern North Atlantic (possibly due to weak mediterranean outflow)
313 and small negative temperature and salinity biases in the Pacific and Indian Ocean. The very deep depth
314 range of 2000-4000 m reveals rather small warming bias for the entire Atlantic and SO.

315 `Fesom_KPP` and `fesom_PP` produced rather small temperature and salinity differences (note different
316 colorbar ranges between 1st & 2nd and 3rd & 4th column), considering the biases with respect to the `WOA18`
317 climatology. Employing `fesom_PP` has the tendency to be slightly warmer almost everywhere in the
318 subsurface layers and slightly saltier especially in the AO and fresher in the surface layer of the subtropical
319 and equatorial ocean compared to using `fesom_KPP`.

320 Fig. 9 shows the difference in temperature (1st column), salinity (2nd column) and vertical diffusivity (3rd



19

321 column) between *cvmix_KPP* and *fesom_KPP* (*cvmix_KPP* minus *fesom_KPP*) averaged over five different
322 depth ranges. The last column presents the *fesom_KPP* vertical diffusivity as a reference. Also here, the
323 temperature and salinity differences are rather small compared to the climatological biases shown in Suppl.
324 2. *cvmix_KPP* has the tendency to produce in the marginal seas of the AO a slightly fresher surface ocean,
325 while the central AO shows an increase in salinity by ~ 0.1 psu.

326 The absolute value of the vertical diffusivity in *fesom_KPP* is larger than that in *cvmix_KPP* in the surface
327 layers as well as in regions of unstable stratification (buoyancy frequency < 0), superimposed on a non-
328 constant background diffusivity as described in Scholz et al., 2019. The different treatment of the squared
329 velocity shear and buoyancy difference with respect to the surface in *cvmix_KPP* leads to a reduction of the
330 vertical diffusivity (3rd column) in the Labrador and Irminger Seas and to an increase in the AO locally by up
331 to one order of magnitude (especially in the deep ocean).

332 The differences in MLD between *fesom_KPP* and *cvmix_KPP* are presented in Fig. 10, where a) and b)
333 show the absolute MLD value for *fesom_KPP* in the northern hemisphere in March and in the southern
334 hemisphere in September respectively. Fig. 10 c) and d) display the corresponding anomalies between
335 *cvmix_KPP* and *fesom_KPP* (*cvmix_KPP*-*fesom_KPP*). The absolute MLD values for *fesom_KPP* in March
336 show high values of up to 3300 m in the entire LS and parts of the Irminger Sea, intermediate values of up to
337 2000 m in the northern and eastern GIN seas and values of ~ 900 m along the eastern continental slope of the
338 North Atlantic. In the southern hemisphere in September, *fesom_KPP* simulates large MLD of ~ 2500 m in
339 the central Weddell Sea and weaker MLD of ~ 500 m in the band of the Antarctic Circumpolar Current
340 (ACC). Compared to the *fesom_KPP*, *cvmix_KPP* leads to a ~ 200 m weaker MLD in the boundary currents
341 of the LS, southern LS and along the northeastern continental slope of the GIN seas, and slightly larger MLD
342 values in the IS and southwestern GIN Seas.

343 Fig. 11 presents the differences in temperature (1st column), salinity (2nd column) and vertical diffusivity K_v
344 (3rd column) between *cvmix_PP* and *fesom_PP* (*cvmix_PP* minus *fesom_PP*) as well as the absolute values
345 of vertical diffusivity for *fesom_PP* (4th column). For the upper two surface depth ranges, *cvmix_PP* shows
346 an overall small warming anomaly, except for the Gulf of Guinea in the 250-500 m depth range where the
347 anomaly is negative. The salinity with *cvmix_PP* has overall slight positive anomalies, except for coastal
348 Arctic areas and the Gulf of Guinea which indicate a slight freshening anomaly when compared to
349 *fesom_PP*. The depth ranges below 500 m show no significant temperature or salinity differences between
350 *cvmix_PP* and *fesom_PP*. The absolute value of K_v in *fesom_PP* shows also larger values all over the
351 surface layer as well as in the areas of unstable stratification similar to *fesom_KPP*, but with a lower
352 magnitude and a more extended region of increased K_v in the LS and IS. The K_v difference between
353 *cvmix_PP* and *fesom_PP* shows sporadically positive values along the coastal Arctic Ocean and in parts of
354 the North Atlantic and GIN Seas. As one would expect, *cvmix_PP* has an order of magnitude larger values in
355 the very deep ocean layer where the background viscosity enters the computation of K_v in *cvmix_PP*.

356 Fig. 12 presents the absolute and anomalous MLD between *fesom_PP* and *cvmix_PP*. The MLD in



21

357 fesom_PP in March is deep in the entire LS and in parts of the IS, but slightly weaker and less spatially
358 extended when compared to fesom_KPP (Fig. 10). The MLD in the GIN seas is very similar between
359 fesom_PP and fesom_KPP. In the southern hemisphere the September MLD in fesom_PP shows a pattern in
360 the central Weddell Sea which is similar to that in fesom_KPP, but shallower by ~500 m. The MLD
361 difference between cvmix_PP and fesom_PP in the northern hemisphere indicates a very heterogeneous
362 pattern for the North Atlantic and in the southern hemisphere an up to ~150 m deeper MLD in the Weddell
363 Sea MLD for cvmix_PP compared to fesom_PP. Overall, the difference in the simulation results induced by
364 the difference in the two implementations of mixing schemes is generally small when considering the model
365 biases relative to observations.

366 3.3.2 Effects of tidal mixing parameterization of Simmons et al. (2004)

367 The tidal mixing parameterization of Simmons et al., (2004) provided by CVMIX has been added to
368 FESOM2.0. This mixing parameterization takes into account effects from internal wave generation due to
369 tides over rough bottom topography. The breaking of internal waves in the vicinity of topographic features
370 excites small-scale turbulence and leads to an enhanced vertical mixing. The tidal mixing parameterization
371 uses a two dimensional map of tidal energy dissipation flux due to bottom drag and energy conversion into
372 internal waves from Jayne and St. Laurent, (2001). It is transformed under consideration of a vertical
373 redistribution function, the modelled buoyancy frequency and a tidal dissipation efficiency and mixing
374 efficiency into a 3D map of diapycnal tidal vertical mixing, which is added to a primary vertical mixing
375 scheme like PP, KPP or TKE. To show the effect of the tidal mixing parameterization we conducted a
376 simulation using both cvmix_KPP and the tidal vertical mixing (cvmix_KPP_{TIDAL}). This simulation will be
377 compared with a control run with cvmix_KPP in which the tidal mixing is not considered. The differences in
378 temperature (1st column), salinity (2nd column) and vertical diffusivity Kv (3rd column) between
379 cvmix_KPP_{TIDAL} and cvmix_KPP averaged over five different depth ranges are presented in Fig. 13. The last
380 column of Fig. 13 shows the cvmix_KPP Kv as a reference. The temperature anomalies of the upper three
381 depth ranges indicate that cvmix_KPP_{TIDAL} is colder especially in the marginal seas of the North Pacific, e.g.
382 Sea of Japan, Sea of Okhotsk and Bering Sea, within the branch of the Gulf Stream (GS) and North Atlantic
383 Current (NAC) as well as in the GIN- and Barents Seas. The Arctic Ocean shows a cooling anomaly for the
384 500-1000 m and 1000-2000 m depth range. In the southern hemisphere the entire Southern Ocean is slightly
385 colder when including the tidal vertical mixing. The tropical and subtropical ocean indicates a slight
386 warming for cvmix_KPP_{TIDAL}.

387 The salinity anomalies between cvmix_KPP_{TIDAL} and cvmix_KPP show a pattern similar to that of the
388 temperature, with a freshening in the marginal seas of the North Pacific, GS, NAC, GIN- and Barents Seas as
389 well as for the Southern Ocean. The upper depth range indicates an increase in salinity for the AO, while the
390 subsurface depth ranges show an AO freshening when including the tidal mixing. The tropical and
391 subtropical ocean shows largely an increase in salinity under cvmix_KPP_{TIDAL}.

392 The difference in vertical diffusivity shows for cvmix_KPP_{TIDAL} an increase by an order of magnitude along

22

11



23

393 all topographic features which is induced by the tidal vertical mixing parameterization. On top of that the
394 central AO shows a reduced vertical diffusivity by at least an order of magnitude for the 250-500 m, 500-
395 1000 m and 1000-2000 m depth ranges, which comes from a change in local hydrography when including
396 the tidal vertical mixing parameterization and the associated difference in the KPP mixing scheme.

397 To further understand the effect of the tidal vertical mixing, Fig. 14 shows the global zonal mean temperature
398 and salinity differences between the case of `cvmix_KPP` and the WOA18 (a, c) and the differences between
399 `cvmix_KPPTIDAL` and `cvmix_KPP` (b, d). The temperature of `cvmix_KPP` shows a rather strong warming bias
400 until 1000 m for the tropical and subtropical ocean as well as until ~2500 m for the ocean north of 50°N with
401 respect to WOA18 (Fig. 14a). The deep ocean features small negative temperature anomalies for the tropical
402 and subtropical ocean and slightly positive biases for the deep SO, when compared to WOA18. The salinity
403 biases of the `cvmix_KPP` case (Fig. 14c) indicate a more heterogeneous but nevertheless similar picture.
404 Also here positive salinity biases can be seen in the tropical and subtropical ocean until around 1000m as
405 well as until ~2500m for the ocean north of 50°N. Looking at the temperature and salinity difference
406 between `cvmix_KPPTIDAL` and `cvmix_KPP`, it can be seen that the tidal mixing of Simmons et al.,
407 (2004) leads to a cooling and freshening of the Southern Ocean and the ocean north of 50°N as well as a
408 warming and salinification for the tropical and subtropical ocean until around 1500m. The deep ocean
409 experiences a general slight warming and freshening due to the inclusion of the tidal mixing
410 parameterization. In general one can summarize that the tidal mixing parameterization of Simmons et al.,
411 (2004) helps to improve some of the biases with respect to WOA18. The last panel in Fig 14e shows the
412 global zonal averaged vertical diffusivity profiles between `cvmix_KPPTIDAL` and `cvmix_KPP` and reveals a
413 general strong increase in K_v along the continental slope in the southern ocean, in the northern hemisphere
414 north of 50°N as well as in the deep ocean interior.

415 To illustrate the effect of Simmons et al., (2004) tidal mixing parameterization onto the MLD, Fig. 15
416 presents the northern hemisphere March (a) and southern hemisphere September (b) MLD in the case of
417 `cvmix_KPP`, and the difference in MLD between `cvmix_KPPTIDAL` and `cvmix_KPP` also for northern
418 hemisphere March (c) and southern hemisphere September (d). In the northern hemisphere in March, tidal
419 mixing leads to an increase in the MLD within the boundary currents of the LS, southern and eastern GIN
420 Seas as well as in the Sea of Okhotsk. In the southern hemisphere September, tidal mixing leads to a
421 significant ~1000 m increase in the Weddell Sea MLD. This significant increase originates largely from
422 enhanced mixing of very cold surface waters along the continental slope of the Weddell Sea due to the tidal
423 mixing parameterization.

424 3.3.3 Effects of Turbulent-Kinetic-Energy (TKE) mixing parameterisation

425 More elaborate parameterizations of the vertical mixing in the ocean can be achieved by using closure
426 schemes of turbulent kinetic energy (TKE) and the associated turbulent mixing within the mixed layer and
427 below. One of these turbulent closure schemes is by Gaspar et al. (1990) that has been implemented via
428 CVMIX (`cvmix_TKE`) into FESOM2.0 based on the work of Eden et al. (2014) and Gutjahr et al. (2020).

24

12



25

429 The turbulence closure scheme requires the solving of the second-order equation for TKE which is closed by
430 connecting the vertical diffusivity with the turbulent kinetic energy and a length scale for its dissipation
431 (Eden et al., 2014). For the background diffusivity we do not use here the latitude and depth dependent
432 background diffusivity as in the previous mixing schemes. Instead, a constant minimum value of TKE is
433 assumed, which takes into account the ocean interior mixing by internal wave breaking. To understand the
434 effect of `cvmix_TKE` on oceanic hydrography, Fig. 16 presents the temperature and salinity biases of
435 `cvmix_TKE` with respect to WOA18 (1st and 3rd column). To relate `cvmix_TKE` to the other vertical mixing
436 schemes (e.g. KPP), the temperature and salinity differences between `fesom_KPP` and `cvmix_TKE` (2nd and
437 4th column) are shown as well. In general, the `cvmix_TKE` temperature and salinity biases with respect to
438 WOA18 look largely very similar to the biases of `fesom_KPP` shown in Supp2. 1 (1st and 3rd column) in
439 terms of the spatial patterns. A closer inspection of temperature and salinity differences between `cvmix_TKE`
440 and `fesom_KPP` (Fig. 18, 2nd and 4th column) reveals that `cvmix_TKE` produces an up to 0.5°C colder ocean
441 within the 0-250 m, 250-500 m and 500-1000 m depth ranges in most of the ocean, a strong warming along
442 the pathway of the NAC and the southern polar front in the South Atlantic, and small warming biases in the
443 AO and SO. The salinity differences between `cvmix_TKE` and `fesom_KPP` indicate a salinification of the
444 AO throughout the 0-250 m, 250-500 m and 500-1000 m depth ranges, but most pronounced in the surface
445 depth range. The surface saline bias largely stems from reduced mixing under sea ice, which shields the
446 ocean from the wind stress, a large source term of TKE. Furthermore, there are positive salinity anomalies in
447 the North Atlantic (in the pathway of the GS and NAC), North Pacific and Southern Ocean, and largely
448 negative salinity anomalies in the southern hemisphere. The temperature and salinity differences between
449 `cvmix_TKE` and `fesom_KPP` in the depth ranges of 1000-2000 m and 2000-4000 m are rather marginal. It
450 should be mentioned that a part of the anomalies described here could also be attributed to the different
451 treatment of the background diffusivity. `fesom_KPP` takes a latitude and depth dependent value (Scholz et
452 al., 2019), while `cvmix_TKE` assumes a constant value of minimum TKE on the surface ($10e-4 \text{ m}^2/\text{s}^2$) and
453 for the interior mixing ($10e-6 \text{ m}^2/\text{s}^2$).

454 **3.3.4 Effects of energy consistent combination of TKE with the Internal Wave Dissipation** 455 **Energy and Mixing (IDEMIX) parameterisation**

456 Besides the standard implementation of vertical background diffusivity in `cvmix_TKE` using a constant
457 minimum value of TKE to parameterize the effect of breaking of internal waves, `cvmix_TKE` also allows for
458 the usage of a more sophisticated parameterization of internal wave breaking when combined with the
459 IDEMIX parameterization (Olbers and Eden, 2013; Eden et al., 2014) which describes the energy transfer
460 from sources towards sinks of internal waves by using a radiative transfer equation of weakly interacting
461 internal waves. The resulting dissipation of energy is then treated as a source term in the turbulent kinetic
462 energy balance equation leading at the end to an energetically more consistent interpretation of the internal
463 ocean mixing process (Eden et al., 2014; Gutjahr et al., 2020). Thereby, IDEMIX solves for the propagation
464 of low-mode internal waves far from their generation sites, which is considered by Fox-Kemper et al., (2019)

26

13



27

465 as one of the most difficult components of the internal wave energy budget. Different from the tidal mixing
466 parameterization of Simmons et al., (2004), which only represents the generation of internal waves by
467 barotropic tides and their breaking at rough topography, IDEMIX considers both the internal waves due to
468 barotropic tides and the internal waves induced by wind-stress fluctuations and exiting at the base of the
469 mixed layer (Gutjahr et al., 2020). The combination of cvmix_TKE and IDEMIX to improve the energetic
470 consistency of ocean models is a rather new approach in the modelling community. It has been evaluated for
471 stand-alone ocean models (Eden et al., 2014; Nielsen et al., 2018; Pollmann et al., 2017) and coupled models
472 (Nielsen et al., 2019). Further, the computed TKE dissipation rates from IDEMIX have been evaluated
473 against observational Argo float-derived dissipation rates by Pollmann et al. (2017) and have been found to
474 be in good agreement (Gutjahr et al., 2019). In this part of the FESOM2 documentation, two FESOM2.0
475 simulations with cvmix_TKE, one with and one without the usage of IDEMIX, are compared to assess the
476 effect of IDEMIX on the modelled hydrography.

477 Fig. 17 presents the temperature (1st column), salinity (2nd column) and vertical diffusivity (3rd column)
478 differences between cvmix_TKE with IDEMIX versus without it, averaged over five different depth layer
479 ranges. As a reference the vertical diffusivity of cvmix_TKE without IDEMIX is also shown in the 4th
480 column. The temperature differences indicate a clear warming of all equatorial and mid-latitude oceans
481 and a cooling in the AO, SO and the marginal seas of the North Pacific throughout almost all the depth
482 ranges, when cvmix_TKE is used with IDEMIX. There is a particularly strong warming in the surface and
483 subsurface depth range of the North Atlantic, in the subsurface depth range of the south Pacific and in the
484 deeper depth ranges of the Indian Ocean. The salinity differences (2nd column) have a similar spatial pattern,
485 showing a rather strong salinification of the equatorial and mid-latitude global oceans and a freshening of
486 the AO, SO and North Pacific from the surface to 500-1000 m depth range. The depth ranges below indicate
487 a predominant general freshening almost everywhere, except for the Mediterranean outflow and Indian
488 Ocean which indicate a slight warming. The differences in the vertical diffusivity between cvmix_TKE with
489 and without IDEMIX are only very small in the upper layer depth range. Therefore, all subsurface depth
490 layers indicate considerable positive vertical diffusivity differences by up to two orders of magnitude
491 especially along all major topographic features as well as in the SO. This shows in particular how IDEMIX
492 parameterizes the vertical mixing due to the breaking of upwards propagating internal wave excited by
493 barotropic tides along the ocean bottom topography but also the vertical mixing related to the internal wave
494 breaking of downward propagating internal waves radiated out of the mixed layer like e.g. in the SO.

495 Fig. 18 presents the global zonal mean temperature and salinity differences of cvmix_TKE with respect to
496 the WOA18 (a, c) as well as the temperature, salinity and vertical diffusivity differences between
497 cvmix_TKE_{IDEMIX} and cvmix_TKE (b, d, e). The zonal mean temperature biases of cvmix_TKE with respect
498 to WOA18 (Fig. 18a) are positive for the upper SO, the equatorial and mid-latitude oceans between 500m
499 until 1000m, and the high-latitude ocean north of 60°N where the warming bias extends nearly from the
500 surface until a depth of ~2500m. A rather weak warming bias is also present for the very deep >2500m SO.

28

14



29

501 General cooling biases can be seen for the equatorial and mid-latitudinal surface oceans, between a depth of
502 ~1000m to 2000m as well as for the very deep ocean. The salinity biases for cvmix_TKE (Fig. 18c) show too
503 high salinities for the high-latitude ocean north of 40°N and for the surface SO. Small salinity biases can be
504 found in the equatorial and mid-latitudinal surface layers as well as around 40°N between ~1000 and 3000
505 m.

506 The temperature differences between cvmix_TKE with and without IDEMIX (Fig. 18b) shows that the
507 IDEMIX leads to a general warming of the equatorial and mid-latitudinal oceans especially between ~500 m
508 and ~2000 m, but a cooling in the northern and southern high-latitude oceans. The salinity differences
509 between cvmix_TKE with and without IDEMIX reveal a similar pattern with an increase in salinity for the
510 equatorial and mid-latitudinal ocean from the surface until a depth ~2000m and a freshening bias in the same
511 depth range for the high-latitudinal oceans and for the entire deep ocean as well.

512 The corresponding vertical diffusivity difference is shown in Fig. 18e. There, using IDEMIX results in an
513 increase in vertical diffusivity along the bottom topographic slopes in the SO and north of 50°N until 70°N.
514 Further, an increase in vertical diffusivity can be observed for almost the entire upper ocean until ~2000 m
515 with deeper reaching positive anomalies between -60°S - 30°S and 30°N - 50°N. A reduction of the vertical
516 diffusivity can be observed for the entire AO from the surface to bottom, for the equatorial and mid-
517 latitudinal deep ocean >3000 m as well as for the deep (>4000 m) SO.

518 The effect of IDEMIX on the MLD is presented in Fig. 19, which shows the northern hemisphere March a)
519 and southern hemisphere September b) cvmix_TKE MLD and the corresponding anomalies between
520 cvmix_TKE with and without IDEMIX. It indicates that the use of IDEMIX leads to an increase in northern
521 hemisphere MLD within the boundary currents of the LS by up to ~1000 m and in the southeastern GIN Seas
522 by up to ~1800 m. In the southern hemisphere September, IDEMIX leads to a significant increase of the
523 Weddell Sea MLD up to ~1800 m. We observe that using cvmix_KPP_{TIDAL} or cvmix_TKE_{IDEMIX} the model
524 cannot maintain the upper halocline in the Weddell Sea. Hence the warm water that shall stay deep is
525 exposed to the surface and the ocean loses heat. It can be well seen from Fig. 14.b and 18.b as blobs of
526 negative temperature differences beneath the surface. As a consequence, the enlarged MLDs in the Weddell
527 Sea appear. We therefore recommend to combine cvmix_KPP_{TIDAL} or cvmix_TKE_{IDEMIX} with the partial
528 bottom cell approach, which has a compensating effect on the stratification in the Weddell Sea (see section
529 3.1 and Suppl. 1) due to improvements of the current circulation in the Weddell Sea.

530 3.4 Implementation of Monin-Obukhov length dependent vertical mixing

531 In this section the effect of the Monin-Obukhov length vertical mixing (MOMIX) of Timmermann and
532 Beckmann (2004) in FESOM2.0 is discussed. In an attempt to decrease the climatological biases especially
533 in the Southern Ocean, which were otherwise prone to significant cooling and salinification (not shown),
534 MOMIX has been implemented into FESOM2.0 as well. MOMIX serves as a parameterisation of the wind
535 driven mixing in the Southern Ocean, effective especially in the melting season, which helps to reduce



31

536 winter deep convection in the Weddell Sea, thus affecting the basin wide ocean- and meridional overturning
537 circulation (Timmermann and Beckmann, 2004). MOMIX computes the Monin-Obukhov length based on
538 heat flux, freshwater flux, wind stress, sea ice concentration and sea ice velocity following the approach of
539 Lemke (1987), and subsequently increases the vertical diffusivity within the Monin-Obukhov length to a
540 value of $0.01\text{m}^2/\text{s}$.

541 Due to its success in reducing the aforementioned mean biases, MOMIX is applied at the moment in
542 FESOM2.0 per default south of -50°S . In the following, the effects of MOMIX are discussed, based on
543 simulation of fesom_KPP and cvmix_TKE each with and without MOMIX.

544 Fig. 20 presents the temperature (1st and 2nd column) and salinity (3rd and 4th column) differences between
545 simulations with and without MOMIX for both the fesom_KPP and cvmix_TKE schemes, averaged over
546 five different depth ranges. Using MOMIX in the Southern Ocean leads to a significant warming of up to
547 1°C for almost the entire Southern Ocean south of -60°S throughout all considered depth ranges, except for
548 the surface depth range of the southern Weddell Sea and subsurface southern Pacific which exhibits cooling
549 anomalies. The warming anomaly is slightly more pronounced for fesom_KPP than cvmix_TKE. The usage
550 of MOMIX in the Southern Ocean leads in fesom_KPP to a warming of the Gulf Stream and to a cooling of
551 the NAC. For cvmix_TKE this behaviour is reversed. The salinity anomalies indicate a freshening for the
552 entire Southern Ocean surface depth range when using MOMIX, while the subsurface depth ranges indicate
553 predominantly a slight increase in salinity, except for the southern Weddell Sea 250-500m depth range.

554 To emphasize the effect of MOMIX on the Weddell Sea MLD, Fig. 21 presents the Southern Ocean
555 September MLD for fesom_KPP (a) and cvmix_TIDAL (b) without MOMIX and the corresponding
556 anomalies with minus without MOMIX (c, d). The MLD for fesom_KPP (a) and cvmix_TKE (b) are very
557 large over the entire Weddell Sea and parts of the Ross Sea. The MLD values are higher and more extended
558 with fesom_KPP than with cvmix_TKE. However, for both vertical mixing schemes without using MOMIX,
559 the MLD values are way too high within the Weddell Sea and Ross Sea. The figures c) and d) visualize what
560 happens with the Southern Ocean MLD for fesom_KPP and cvmix_TKE when MOMIX is used. Especially
561 for fesom_KPP, MOMIX leads to a significant decrease in the MLD in almost the entire Weddell Sea of up
562 to ~ 3000 m, except for the southwestern Weddell Sea close to the continental shelf which exhibits an
563 increase in MLD. Also the large MLD patch in the Ross Sea becomes strongly reduced when using MOMIX.

564 Both fesom_KPP and cvmix_TKE face the same pattern in MLD reduction when using MOMIX, only the
565 magnitude in the MLD decrease is larger in fesom_KPP than in cvmix_TKE.

566 Since MOMIX has a rather strong effect in reducing the Weddell Sea open-ocean deep-water formation it
567 will also consequently affect the formation of Antarctic Bottom Water (AABW) and the Meridional
568 Overturning Circulation (MOC). Fig. 22 shows the fesom_KPP global (a), Atlantic (b) and Pacific (c) MOC
569 when MOMIX is switched off and the difference from the case with MOMIX (bottom row). It can be seen
570 that on a global but also basin-wide scale, the use of MOMIX leads to a reduction in the strength of the
571 AABW, in the Atlantic by ~ 0.6 Sv and in the Pacific by up to ~ 1.7 Sv. Also the strength of the upper AMOC



33

572 cell is reduced by ~ 1 Sv when using MOMIX. We conclude that using MOMIX helps to alleviate the
573 problem of large MLDs in the Weddell Sea which we addressed above. Hence, the options `cvmix_KPPTIDAL`
574 or `cvmix_TKEIDEMIX` are strongly recommended to be used in combination with MOMIX, which is per
575 default active only South of -50°S .

576

577 **4 Discussion and Conclusions**

578 This paper describes the two new features -- partial cells and embedded sea ice introduced to FESOM2.0 and
579 the implementation of the vertical mixing library CVMIX (`cvmix_PP`, `cvmix_KPP`, `cvmix_TKE`, `IDEMIX`
580 and `cvmix_TIDAL`), together with the elaboration of the effect of MOMIX. These new features expand the
581 functionality of FESOM2.0, its applicability and its ability to be better compared to other state of the art
582 ocean general circulation models. With its model components implemented, FESOM2.0 is mature for its
583 practical applications and holds its leading role in the competition of the global unstructured ocean models.

584 We demonstrate the effect of using partial cells by comparing them against the full cell approach. It is shown
585 that partial cells lead to an improved representation of the Gulf Stream branch, with a reduction in the cold
586 bias in the northwest corner of the North Atlantic associated with an improved NAC pathway. Further,
587 partial cells lead to a “northwest corner like” meridional deflection of the NAC between -30°W and -15°W
588 which is still too far east, but leads to an improved representation in a rather coarse configuration which
589 would otherwise be dominated by a rather zonal NAC. Partial cells also lead to a general speed up of the
590 boundary currents shown as an example for the North Atlantic.

591 The improvement of the NAC pathway and the speedup of the boundary currents especially in the subpolar
592 gyre by using partial cells is described by a variety of publications (e.g. Barnier et al., 2006; Käse et al.,
593 2001; Myers, 2002). Besides all its advantages, partial cells also harbor the risk of increasing the existing
594 biases, like in our coarse configuration the deep Arctic warm bias, which is largely inherited from the
595 Atlantic Water inflow branch that expands too deep. The tendency of partial cells to increase the velocity in
596 the boundary currents leads to an enhancement of the Atlantic Water inflow to the Arctic Ocean. As the
597 temperature in the Arctic Atlantic Water layer is already overestimated without using partial cells, the warm
598 bias becomes even larger when partial cells are used. However, this is not the principle drawback of partial
599 cells, but rather an issue of model tuning for the pan-Arctic region, which is part of our on-going work (for
600 example, evaluating different numerical schemes of momentum viscosity). In the southern hemisphere, using
601 partial cells leads to a significant reduction of the otherwise rather high MLD in the Weddell Sea. Regarding
602 the configuration used in this paper, using partial cells leads to a strengthening of the warm deep water
603 current (Vernet et al. 2019) that crosses the Weddell Sea interior. Thus it enhances the local stratification
604 (see Suppl. 1 white arrow) and reduces vertical convection. It can be summarized that the usage of partial
605 cells clearly improves the general circulation within FESOM2.0 and that the benefits outweigh the
606 drawbacks.

34



35

607

608 The second feature that was presented, is the effect of embedded sea ice vs. the standard case of levitating
609 sea ice. Embedded sea ice allows for a further step towards a more realistic and physical ocean-sea ice
610 interaction by adding the sea ice loading to the ocean pressure. This has the potential of increasing ocean
611 variability especially near the sea ice edge. Our results indicate that the embedded sea ice has only a minor
612 effect on the sea ice distribution itself. Nevertheless the effect is the strongest for the Northern Hemisphere
613 summer, when the sea ice edge retracts towards the Arctic Ocean interior. Here embedded sea ice leads to an
614 up to 9% increase in the sea ice concentration in the eastern Arctic Ocean marginal seas, which also leads to
615 an increase in the bias of the sea ice edge, and to a 6% decrease in the marginal seas of the western Arctic
616 Ocean, which slightly reduces the sea ice extent bias there. The effect of embedded sea ice on the
617 hydrography of the Arctic Ocean is much more significant, with an increase in temperature and salinity of up
618 to 0.5°C and 0.1psu, respectively through most of the upper 1000 m. The increase in temperature and salinity
619 is connected to a particular increase of the boundary currents especially along the eastern boundaries of the
620 Eurasian Basin but also to a strengthening of the cyclonic current along the Lomonosov Ridge, which was
621 otherwise rather weakly represented in the levitating sea ice case. The deficiencies of the Arctic Ocean
622 currents representation in our model configuration can be partially attributed to the rather coarse resolution.
623 However, with embedded sea ice we seem to be able to at least partly counteract the effect of low resolution
624 and improve the Arctic Ocean current structure at rather low costs. We note that embedded sea ice could also
625 deteriorate the model results in some cases. Since the boundary currents around the Eurasian Basin get
626 enhanced, the already existing Atlantic Water layer biases get enhanced. However, as mentioned above, this
627 is an issue of model tuning with this coarse resolution setup, not a drawback of embedded sea ice itself.

628

629 To further expand the functionality and comparability of FESOM2.0 we implemented the vertical mixing
630 library CVMIX and its components, which in our implementation include `cvmix_PP`, `cvmix_KPP`,
631 `cvmix_TIDAL`, `cvmix_TKE` and `cvmix_TKE+IDEMIX`. At first, the vertical mixing parameterizations
632 `fesom_KPP` and `fesom_PP`, which have been already implemented in FESOM2.0, are briefly evaluated. It is
633 shown that `fesom_PP` produces a slightly colder tropical and subtropical but warmer polar oceans on the
634 surface, with a largely warmer ocean below the surface layer depth range, when compared to `fesom_KPP`.
635 This makes between these two, `fesom_KPP` the preferred vertical mixing option at least in terms of mean
636 temperature biases. In terms of salinity biases, `fesom_PP` performs better in the surface and subsurface AO
637 as well as in the equatorial Atlantic and Indian Ocean, while otherwise `fesom_KPP` indicates smaller biases.
638 In the next instance, `fesom_KPP` and `cvmix_KPP` have been compared to each other, since there are slight
639 differences in their implementation. The difference in implementation leads only to minor differences in
640 temperature throughout all considered depth ranges. Regarding the salinity differences, `cvmix_KPP` produces
641 a considerably fresher surface AO compared to `fesom_KPP`, which is attributed to a reduced near surface
642 vertical diffusivity in `cvmix_KPP` that leads to an over-stabilisation of the AO halocline. This enhances the



37

643 mean salinity bias in that region. In terms of vertical diffusivity, `cvmix_KPP` has the tendency to produce by
644 up to one order of magnitude lower value (especially in the very deep depth range) in the main convection
645 areas of Labrador Sea and Greenland Sea, throughout all considered depth ranges, accompanied by increased
646 diffusivity in the subsurface of the Arctic Ocean. The reduced diffusivity in the main convection areas is
647 attributed to the different treatment of the shear- and buoyancy difference with respect to the surface in
648 `cvmix_KPP` that leads to a reduction of the local ocean boundary layer depth and to slightly reduced
649 maximum MLD in Labrador and Greenland Sea, while the maximum MLD in the Weddell Sea becomes
650 slightly enhanced, when using `cvmix_KPP` over `fesom_KPP`.

651 Since the implementation of `cvmix_PP` and `fesom_PP` are also slightly different, we also compare them.
652 Although the produced diffusivities between `cvmix_PP` and `fesom_PP` are very similar, `cvmix_PP` indicates
653 a further warming and salinification in the surface and 250-500 m depth ranges except for the upwelling
654 region in the Gulf of Guinea which indicates a cooling and freshening and the surface depth range of the
655 Arctic Ocean where it creates a predominant freshening, when compared the `fesom_PP`. The MLD values
656 indicate that `cvmix_PP` leads in FESOM2.0 to a slightly stronger convection in the Weddell Sea. The
657 differences between `fesom_PP` and `cvmix_PP` are related to the different treatment of the background
658 coefficient for viscosity when computing the diffusivity see Pacanowski and Philander (1981).

659 The effect of implementing `cvmix_TIDAL` in combination with `cvmix_KPP` was further assessed.
660 `cvmix_TIDAL` serves here as a resourceful way to heterogenize the effect of tidally induced internal wave
661 breaking that is otherwise homogenized in a constant or latitude dependent value for the background
662 diffusivity. Using `cvmix_TIDAL` clearly leads to an enhancement of the vertical diffusivity along the slopes
663 of the bottom topography, where tidally related internal wave breaking is induced. This leads especially in
664 the high-latitude marginal seas, e.g. Sea of Okhotsk and Bering Sea but also Arctic Ocean and Southern
665 Ocean, to a decrease in temperature and salinity due to the enhanced mixing along their shelves. This enables
666 `cvmix_TIDAL` to improve some of the existing local temperature and salinity biases within FESOM2.0 at
667 rather low computational costs. However, the enhanced vertical diffusivity along the shelf of the Weddell
668 Sea weakens the stratification and leads to a further increase in the MLD of the Weddell Sea of up to 1000
669 m.

670 Further, the implications of TKE vertical mixing parameterisation in FESOM2.0, added by Eden et al. (2014)
671 and Gutjahr et al. (2020) to the CVMIX library, was evaluated based on a comparison with `fesom_KPP`. It is
672 shown that the mean temperature and salinity differences between `cvmix_TKE` (Fig. 17) and `fesom_KPP`
673 (Fig. 9) show very similar patterns. `cvmix_TKE` tends to produce a generally colder tropical and
674 extratropical ocean together with slightly warmer polar oceans when compared to `fesom_KPP`. The salinity
675 differences between `cvmix_TKE` and `fesom_KPP` shows that `cvmix_TKE` tends to produce a significantly
676 saltier surface layer AO, revealing a much smaller salinity bias for the Arctic Ocean interior. This is largely
677 connected to enhanced surface vertical mixing along the Arctic Ocean shelf break (not shown) within
678 `cvmix_TKE`, that helps to partly destabilize the AO halocline. The improvement of the Arctic Ocean

38

19



39

679 hydrography when using `cvmix_TKE` is also found by Gutjahr et al. (2020) in the coupled ocean-atmosphere
680 Max Planck Institute Earth System Model (MPI-ESM1.2). Further, `cvmix_TKE` leads to a salinity increase in
681 the entire North Atlantic and northwest Pacific marginal seas, while the southern hemisphere, except for the
682 Southern Ocean, shows a freshening when compared to `fesom_KPP`. The reduced temperatures and salinities
683 in the tropics and extratropics when using `cvmix_TKE` are connected to the reduced vertical mixing.
684 However the regions of strong vertical shear, e.g. the branch of the Gulf Stream and NAC as well as
685 Southern Ocean show stronger vertical mixing in `cvmix_TKE`, when compared to `fesom_KPP` (not shown),
686 which is accompanied by positive temperature and salinity anomalies between `cvmix_TKE` and `fesom_KPP`.
687 Following the comparison of `cvmix_TKE` and `fesom_KPP`, a side by side comparison of `cvmix_TKE` with
688 and without IDEMIX was carried out. Here IDEMIX provides an alternative formulation of the background
689 diffusivity in `cvmix_TKE` using a radiative transfer equation of weakly interacting internal waves (Olbers
690 and Eden 2013), where energy is transferred from sources of internal waves to wave sinks, such as the
691 breaking of internal waves, which provide a source for TKE, leading to an energetically more consistent
692 treatment of internal mixing (Eden et al. 2014). As compared to the tidal background mixing
693 parameterization of Simmons et al (2004), IDEMIX allows not only for the generation of internal waves by
694 barotropic tides interacting with marine topography, but also for their propagation in the horizontal and
695 vertical directions away from region of generation and their damping due to wave-wave interaction or
696 interaction with the continental shelf. Further, IDEMIX allows for the excitation of internal waves at the base
697 of the mixed layer by high frequency wind forcing (Eden et al. 2014).
698 The combined TKE + IDEMIX approach was already applied in a couple of publications (Eden et al. 2014,
699 Nielsen et al. 2018, Gutjahr et al. 2020). It was shown in Pollmann et al. 2017 that TKE dissipation rates
700 from the combined TKE+IDEMIX approach are comparable to dissipation rates estimated from Argo floats.
701 In FESOM2.0, the usage of TKE+IDEMIX leads to a significant increase in the tropical and extratropical
702 and to a decrease in the high-latitude temperature and salinity over depth when compared to the case of only
703 using `cvmix_TKE`. These differences compensate for some of the biases in the surface and intermediate
704 depth ranges when IDEMIX is not used. The usage of IDEMIX leads to an enhanced heterogeneous
705 representation of vertical mixing especially below the mixed layer along the continental shelves and
706 topographic slopes. However the temperature gain for the deeper depth ranges below 1000 m seems to be
707 strongly overestimated when using `cvmix_TKE+IDEMIX`, hinting at a too strong vertical mixing in the deep
708 ocean. When it comes to the MLD, `cvmix_TKE+IDEMIX` leads in the northern hemisphere to a significant
709 increase in the MLD along the Labrador Sea boundary currents and in the southern GIN seas, which can be
710 attributed to the enhanced mixing along the continental slope of the North Atlantic and in the vicinity of the
711 overflow regions. In the southern hemisphere using IDEMIX leads to an enhancement of the vertical
712 diffusivity along the continental slope of the Weddell Sea. This leads to an enhanced mixing of cold and
713 salty waters, which further reduces the stratification and significantly increases the MLD of the Weddell Sea
714 and to a rather overestimation of the otherwise already high MLD values.



41

715 This is in contrast to the findings of Gutjahr et al. 2020, who found that in their coupled MPI-ESM1.2
716 simulation, IDEMIX led to a reduction of the vertical mixing in the Weddell Sea allowing for more local
717 stratification. On possibility to overcome the lack of performance of IDEMIX but also of cvmix_TIDAL in
718 the Southern Ocean and Weddell Sea could be its combination with partial bottom cells, which had the
719 tendency to significantly reduce the deep convection in the Weddell Sea. At this point it needs further studies
720 also with FESOM2.0 to analyse the different behaviour of IDEMIX that could be influenced by local
721 resolution, coupled ocean-atmosphere feedback or just different background water mass structure.
722 Nevertheless, the achievable energetic consistency with the combined cvmix_TKE+IDEMIX approach is an
723 interesting feature that should find more applications in the ocean modelling community, although there is
724 still some way to go to better understand and improve its integration.

725 The last part in this paper deals with the vertical mixing parameterisation MOMIX of Timmermann and
726 Beckmann, (2004) in FESOM2.0 that helped us to overcome some major biases in the model. Since the very
727 beginning of FESOM2.0 the model suffered from a severe cooling and salinification bias in the Southern
728 Ocean and marginal seas around Antarctica, that was accompanied by a strongly overestimated MLD values
729 and too weak stratification in the Weddell Sea. It is shown here that applying MOMIX south of -50°S helped
730 to significantly reduce the biases and bring the MLD depth values in the Weddell Sea into a reasonable
731 range. MOMIX increases the vertical diffusivity within the depth range of the Monin-Obukhov mixing
732 length. This helps the warmer and fresher surface water masses from the melting season to connect with
733 colder and saltier subsurface water masses from the freezing season and thus increase the stratification and
734 reduce the vertical convection. The reason why FESOM2.0 in the Southern Ocean is so dependent on
735 MOMIX, which was not the case with FESOM1.4, needs further research.

736 To summarize, this paper is the second part of the documentation of the development of important key
737 components of FESOM2.0 in a realistic global model configuration. We described the implementation of
738 partial cells and embedded sea ice and their impact on the modelled hydrography. Furthermore, we briefly
739 described the already existing vertical mixing parameterisation of fesom_KPP and fesom_PP as well as the
740 newly introduced mixing parameterization of cvmix_PP, cmix_KPP, cmix_TIDAL, cvmix_TKE and
741 cvmix_TKE+IDEMIX that came with the incorporation of the vertical mixing library CVMIX into
742 FESOM2.0.

743 **5 Code availability**

744 The FESOM2.0 version used to carry out the simulations reported here is available on zenodo through
745 <https://doi.org/10.5281/zenodo.4742242>. The used mesh, as well as the temperature, salinity and vertical
746 velocity (for the calculation of the MOC) data of all conducted simulations, can be found under
747 https://swiftbrowser.dkrz.de/tcl_s/hituvPNH3xwiIy/FESOM2.0_evaluation_part2_scholz_etal. Simulated
748 results can of course also be obtained from the authors upon request. Mesh partitioning in FESOM2.0 is
749 based on a METIS version 5.1.0 package developed at the Department of Computer Science and Engineering

42

21



43

750 at the University of Minnesota (<http://glaros.dtc.umn.edu/gkhome/views/metis>, last access: 18 November
751 2019). METIS and the pARMS solver (Li et al., 2003) present separate libraries which are freely available
752 subject to their licenses. The Polar Science Center hydrographic climatology (Steele et al., 2001) used for
753 model initialization and the CORE-II atmospheric forcing data (Large and Yeager, 2009) is freely available
754 online. The vertical mixing library CVMIX is freely available from <https://github.com/CVMix/CVMix-src> or
755 <https://doi.org/10.5281/zenodo.1000801>

756

757 Author contributions

758 SD, DS, PS and NK worked on the development of the FESOM2.0 model code and the tuning of the model.
759 All simulations shown in this paper were carried out by PS who were also responsible for preparing the basic
760 manuscript. QW, SD, NK, DS and TJ have contributed to the final version of the manuscript.

761 Acknowledgements

762 This paper is a contribution to the project S2: Improved parameterisations and numerics in climate models,
763 S1: Diagnosis and Metrics in Climate Models and M5: Reducing spurious diapycnal mixing in ocean models
764 of the Collaborative Research Centre TRR 181 “Energy Transfer in Atmosphere and Ocean” funded by the
765 Deutsche Forschungsgemeinschaft (DFG, German Research Foundation) – project no. 274762653, and the
766 Helmholtz initiative REKLIM (Regional Climate Change). This study has benefited from funding from the
767 Initiative and Networking Fund of the Helmholtz Association through the project “Advanced Earth System
768 Modelling Capacity (ESM)”. Dmitry Sein was also supported in the framework of the state assignment of the
769 Ministry of Science and Higher Education of Russia (№0128-2021-0014).

770 References

771

- 772 Adcroft, A. and Campin, J.-M.: Rescaled height coordinates for accurate representation of free-surface flows in ocean
773 circulation models, *Ocean Model.*, 7(3–4), 269–284, doi:10.1016/j.ocemod.2003.09.003, 2004.
- 774 Adcroft, A., Hill, C. and Marshall, A. J.: Representation of topography by shaved cells in a height coordinate ocean
775 model, *Mon. Weather Rev.*, 125(9), 2293–2315, doi:10.1175/1520-0493(1997)125<2293:ROTBSC>2.0.CO;2, 1997.
- 776 Barnier, B., Madec, G., Penduff, T., Molines, J.-M., Treguier, A., Le Sommer, J., Beckmann, A., Biastoch, A., Böning,
777 C., Dengg, J., Derval, C., Durand, E., Gulev, S., Remy, E., Talandier, C., Theetten, S., Maltrud, M., McClean, J. and De
778 Cuevas, B.: Impact of partial steps and momentum advection schemes in a global ocean circulation model at eddy-
779 permitting resolution, *Ocean Dyn.*, 56(5–6), 543–567, doi:10.1007/s10236-006-0082-1, 2006.
- 780 Campin, J. M., Marshall, J. and Ferreira, D.: Sea ice-ocean coupling using a rescaled vertical coordinate z^* , *Ocean*
781 *Model.*, 24(1–2), 1–14, doi:10.1016/j.ocemod.2008.05.005, 2008.
- 782 Cavalieri, D. J., Parkinson, C. L., Gloersen, P. and Zwally, H. J.: ea Ice Concentrations from Nimbus-7 SMMR and



- 45
- 783 DMSP SSM/I-SSMIS Passive Microwave Data, Version 1. [Indicate subset used], , doi:10.5067/8GQ8LZQVL0VL,
784 1996.
- 785 Cox, M. D.: A numerical ocean model with improved bottom topographic representation, GFDL/NOAA Tech. Rep., 27
786 pp. [Available from Princet. Univ. Princeton, New Jersey 08540.], 1977.
- 787 Danilov, S., Sidorenko, D., Wang, Q. and Jung, T.: The Finite-volumE Sea ice–Ocean Model (FESOM2), Geosci.
788 Model Dev., 10(2), 765–789, doi:10.5194/gmd-10-765-2017, 2017.
- 789 Eden, C. and Olbers, D.: An energy compartment model for propagation, nonlinear interaction, and dissipation of
790 internal gravity waves, J. Phys. Oceanogr., 44(8), 2093–2106, doi:10.1175/JPO-D-13-0224.1, 2014.
- 791 Eden, C., Czeschel, L. and Olbers, D.: Toward Energetically Consistent Ocean Models, J. Phys. Oceanogr., 44, 3160–
792 3184, doi:10.1175/JPO-D-13-0260.1, 2014.
- 793 Ferrari, R., Griffies, S. M., Nurser, A. J. G. and Vallis, G. K.: A boundary-value problem for the parameterized
794 mesoscale eddy transport, Ocean Model., 32(3–4), 143–156, doi:10.1016/j.ocemod.2010.01.004, 2010.
- 795 Fox-kemper, B., Adcroft, A., Böning, C. W., Chassignet, E. P., Gerdes, R., Greatbatch, R. J., Griffies, S. M. and
796 Hallberg, R. W.: Challenges and Prospects in Ocean Circulation Models, , 6(February), 1–29,
797 doi:10.3389/fmars.2019.00065, 2019.
- 798 Fox-Kemper, B. and Menemenlis, D.: Can large eddy simulation techniques improve mesoscale rich ocean models?, in
799 Ocean Modeling in an Eddying Regime, Volume 177, edited by M. W. Hecht and H. Hasumi, pp. 319–337., 2008.
- 800 Gaspar, P., Goris, Y. G. R. I. and Lefevre, J.: A Simple Eddy Kinetic Energy Model for Simulations of the Oceanic
801 Vertical Mixing ' Tests at Station Papa and Long-Term Upper Ocean Study Site, , 95, 179–193, 1990.
- 802 Gent, P. R. and McWilliams, J. C.: Isopycnal Mixing in Ocean Circulation Models, J. Phys. Oceanogr., 20(1), 150–155,
803 doi:10.1175/1520-0485(1990)020<0150:IMIOCM>2.0.CO;2, 1990.
- 804 Gent, P. R., Willebrand, J., McDougall, T. J. and McWilliams, J. C.: Parameterizing Eddy-Induced Tracer Transports in
805 Ocean Circulation Models, J. Phys. Oceanogr., 25(4), 463–474, doi:10.1175/1520-
806 0485(1995)025<0463:PEITTI>2.0.CO;2, 1995.
- 807 Griffies, S. M., Böning, C., Bryan, F. O., Chassignet, E. P., Gerdes, R., Hasumi, H., Hirst, A., Treguier, A. M. and
808 Webb, D.: Developments in ocean climate modelling, Ocean Model., 2(3–4), 123–192, doi:10.1016/s1463-
809 5003(00)00014-7, 2000.
- 810 Griffies, S. M., Levy, M., Adcroft, A. J., Danabasoglu, G., Hallberg, R. W., Jacobsen, D., Large, W. and Ringler, T.:
811 Theory and numerics of the Community Ocean Vertical Mixing (CVMix) project., 2015.
- 812 Gutjahr, O., Putrasahan, D., Lohmann, K., Jungclaus, J. H., Von Storch, J. S., Brüggemann, N., Haak, H. and Stössel,
813 A.: Max Planck Institute Earth System Model (MPI-ESM1.2) for the High-Resolution Model Intercomparison Project
814 (HighResMIP), Geosci. Model Dev., 12(7), 3241–3281, doi:10.5194/gmd-12-3241-2019, 2019.
- 815 Gutjahr, O., Brüggemann, N., Haak, H., Jungclaus, J. H. Putrasahan, D. A. Lohmann, K. and von Storch, J.-S.:
816 Comparison of ocean vertical mixing schemes in the Max Plank Institute Earth System Model (MPI-ESM1.2), Geosci.
817 Model Dev., in review, doi:https://doi.org/10.5194/gmd-2020-202, 2020.
- 818 Ilicak, M., Drange, H., Wang, Q., Gerdes, R., Aksenov, Y., Bailey, D., Bentsen, M., Biastoch, A., Bozec, A., Böning,
819 C., Cassou, C., Chassignet, E., Coward, A. C., Curry, B., Danabasoglu, G., Danilov, S., Fernandez, E., Fogli, P. G.,
820 Fujii, Y., Griffies, S. M., Iovino, D., Jahn, A., Jung, T., Large, W. G., Lee, C., Lique, C., Lu, J., Masina, S., George
821 Nurser, A. J., Roth, C., Salas y Mélia, D., Samuels, B. L., Spence, P., Tsujino, H., Valcke, S., Voldoire, A., Wang, X.
822 and Yeager, S. G.: An assessment of the Arctic Ocean in a suite of interannual CORE-II simulations. Part III:
823 Hydrography and fluxes, Ocean Model., 100, 141–161, doi:10.1016/j.ocemod.2016.02.004, 2016.



47

- 824 Jayne, S. R. and St. Laurent, L. C.: Tidal Dissipation over Rough, *Geophys. Res. Lett.*, 28(5), 811–814, 2001.
- 825 Käse, R. H., Biastoch, A. and Stammer, D. B.: On the mid-depth circulation in the Labrador and Irminger Seas,
826 *Geophys. Res. Lett.*, 28(18), 3433–3436, doi:10.1029/2001GL013192, 2001.
- 827 Large, W. G. and Yeager, S. G.: The global climatology of an interannually varying air - Sea flux data set, *Clim. Dyn.*,
828 33(2–3), 341–364, doi:10.1007/s00382-008-0441-3, 2009.
- 829 Large, W. G., McWilliams, J. C. and Doney, S. C.: Oceanic vertical mixing: A review and a model with a nonlocal
830 boundary layer parameterization, *Rev. Geophys.*, 32(4), 363, doi:10.1029/94RG01872, 1994.
- 831 Lemke, P.: A coupled one-dimensional sea ice-ocean model, , 92(C12), 164–172,
832 doi:https://doi.org/10.1029/JC092iC12p13164, 1987.
- 833 Locarnini, R. A., Mishonov, A. V., Baranova, O. K., Boyer, T. P., Zweng, M. M., Garcia, H. E., Reagan, J. R., Seidov,
834 D., Weathers, K., Paver, C. R. and Smolyar, I.: World Ocean Atlas 2018, Volume 1: Temperature, A. Mishonov Tech.
835 Ed.; NOAA Atlas NESDIS 81, 52, 2018.
- 836 Maier-Reimer, E., Mikolajewicz, U. and Hasselmann, K.: Mean circulation of the Hamburg LSG OGCM and its
837 sensitivity to the thermohaline surface forcing, *J. Phys. Oceanogr.*, 23(4), 731–757, doi:10.1175/1520-
838 0485(1993)023<0731:MCOTHL>2.0.CO;2, 1993.
- 839 Myers, P. G.: SPOM: A regional model of the sub-polar north Atlantic, *Atmos. - Ocean*, 40(4), 445–463,
840 doi:10.3137/ao.400405, 2002.
- 841 Nielsen, S. B., Jochum, M., Eden, C. and Nuterman, R.: An energetically consistent vertical mixing parameterization in
842 CCSM4, *Ocean Model.*, 127, 46–54, doi:10.1016/j.ocemod.2018.03.002, 2018.
- 843 Nielsen, S. B., Jochum, M., Pedro, J. B., Eden, C. and Nuterman, R.: Two-Timescale Carbon Cycle Response to an
844 AMOC Collapse, *Paleoceanogr. Paleoclimatology*, 34(4), 511–523, doi:10.1029/2018PA003481, 2019.
- 845 Olbers, D. and Eden, C.: A Global Model for the Diapycnal Diffusivity Induced by Internal Gravity Waves, , 1759–
846 1779, doi:10.1175/JPO-D-12-0207.1, 2013.
- 847 Pacanowski, R. C. and Gnanadesikan, A.: Transient response in a Z-level ocean model that resolves topography with
848 partial cells, *Mon. Weather Rev.*, 126(12), 3248–3270, doi:10.1175/1520-0493(1998)126<3248:TRIAZL>2.0.CO;2,
849 1998.
- 850 Pacanowski, R. C. and Philander, S. G. H.: Parameterization of Vertical Mixing in Numerical Models of Tropical
851 Oceans, *J. Phys. Oceanogr.*, 11(11), 1443–1451, doi:10.1175/1520-0485(1981)011<1443:POVMIN>2.0.CO;2, 1981.
- 852 Pollmann, F., Eden, C. and Olbers, D.: Evaluating the Global internal wave model IDEMIX using finestructure
853 methods, *J. Phys. Oceanogr.*, 47(9), 2267–2289, doi:10.1175/JPO-D-16-0204.1, 2017.
- 854 Redi, M. H.: Oceanic Isopycnal Mixing by Coordinate Rotation, *J. Phys. Oceanogr.*, 12(10), 1154–1158,
855 doi:10.1175/1520-0485(1982)012<1154:OIMBCR>2.0.CO;2, 1982.
- 856 Robertson, R. and Dong, C.: An evaluation of the performance of vertical mixing parameterizations for tidal mixing in
857 the Regional Ocean Modeling System (ROMS), *Geosci. Lett.*, 6(1), 1–18, doi:10.1186/s40562-019-0146-y, 2019.
- 858 Rousset, C., Vancoppenolle, M., Madec, G., Fichefet, T., Flavoni, S., Barthélemy, A., Benschila, R., Chanut, J., Levy,
859 C., Masson, S. and Vivier, F.: The Louvain-La-Neuve sea ice model LIM3.6: Global and regional capabilities, *Geosci.
860 Model Dev.*, 8(10), 2991–3005, doi:10.5194/gmd-8-2991-2015, 2015.
- 861 Scholz, P., Sidorenko, D., Gurses, O., Danilov, S., Koldunov, N., Wang, Q., Sein, D., Smolentseva, M., Rakowsky, N.
862 and Jung, T.: Assessment of the Finite-volume Sea ice-Ocean Model (FESOM2.0) -- Part 1: Description of selected key
863 model elements and comparison to its predecessor version, *Geosci. Model Dev.*, 12(11), 4875–4899, doi:10.5194/gmd-
864 12-4875-2019, 2019.



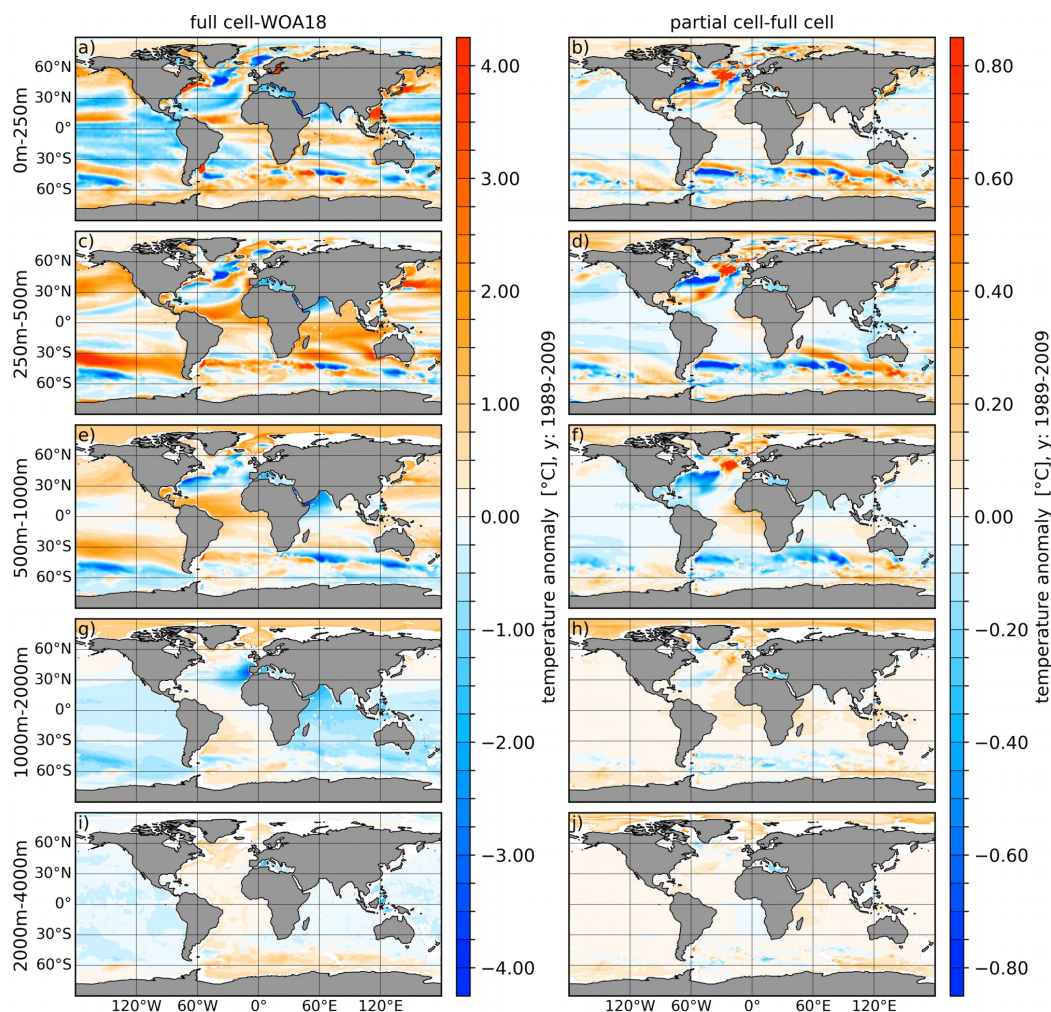
49

- 865 Semmler, T., Danilov, S., Gierz, P., Goessling, H. F., Hegewald, J., Hinrichs, C., Koldunov, N., Khosravi, N., Mu, L.,
866 Rackow, T., Sein, D. V., Sidorenko, D., Wang, Q. and Jung, T.: Simulations for CMIP6 With the AWI Climate Model
867 AWI-CM-1-1, *J. Adv. Model. Earth Syst.*, 12(9), 1–34, doi:10.1029/2019MS002009, 2020.
- 868 Semtner, A. J. and Mintz, Y.: Numerical simulation of the Gulf Stream and mid-ocean eddies., *J. Phys. Oceanogr.*, 7(2,
869 Mar. 1977), 208–230, doi:10.1175/1520-0485(1977)007<0208:nsotgs>2.0.co;2, 1977.
- 870 Shchepetkin, A. F.: A method for computing horizontal pressure-gradient force in an oceanic model with a nonaligned
871 vertical coordinate, *J. Geophys. Res.*, 108(C3), 3090, doi:10.1029/2001JC001047, 2003.
- 872 Simmons, H. L., Jayne, S. R., St, L. C. and Weaver, A. J.: Tidally driven mixing in a numerical model of the ocean
873 general circulation, , 6, 245–263, doi:10.1016/S1463-5003(03)00011-8, 2004.
- 874 Steele, M., Morley, R. and Ermold, W.: PHC: A global ocean hydrography with a high-quality Arctic Ocean, *J. Clim.*,
875 14(9), 2079–2087, doi:10.1175/1520-0442(2001)014<2079:PAGOHW>2.0.CO;2, 2001.
- 876 Timmermann, R. and Beckmann, A.: Parameterization of vertical mixing in the Weddell Sea, *Ocean Model.*, 6(1), 83–
877 100, doi:10.1016/S1463-5003(02)00061-6, 2004.
- 878 Van Roekel, L., Adcroft, A. J., Danabasoglu, G., Griffies, S. M., Kauffman, B., Large, W., Levy, M., Reichl, B. G.,
879 Ringler, T. and Schmidt, M.: The KPP Boundary Layer Scheme for the Ocean: Revisiting Its Formulation and
880 Benchmarking One-Dimensional Simulations Relative to LES, *J. Adv. Model. Earth Syst.*, 10(11), 2647–2685,
881 doi:10.1029/2018MS001336, 2018.
- 882 Vernet, M., Geibert, W., Hoppema, M., Brown, P. J., Haas, C. and Hellmer, H. H.: The Weddell Gyre , *Southern*
883 *Ocean : Present Knowledge and Future Challenges Reviews of Geophysics*, *Rev. Geophys.*, 57, 623–708,
884 doi:10.1029/2018RG000604, 2019.
- 885 Wang, Q., Danilov, S., Sidorenko, D., Timmermann, R., Wekerle, C., Wang, X., Jung, T. and Schröter, J.: The Finite
886 Element Sea Ice-Ocean Model (FESOM) v.1.4: formulation of an ocean general circulation model, *Geosci. Model Dev.*,
887 7(2), 663–693, doi:10.5194/gmd-7-663-2014, 2014.
- 888
889 Zweng, M. M., Reagan, J. R., Seidov, D., Boyer, T. P., Locarnini, R. A., Garcia, H. E., Mishonov, A. V., Baranova, O.
890 K., Weathers, K., Paver, C. R. and Smolyar, I.: *World Ocean Atlas 2018, Volume 2: Salinity*, A. Mishonov Tech. Ed.;
891 NOAA Atlas NESDIS 82, 50, 2018.

892



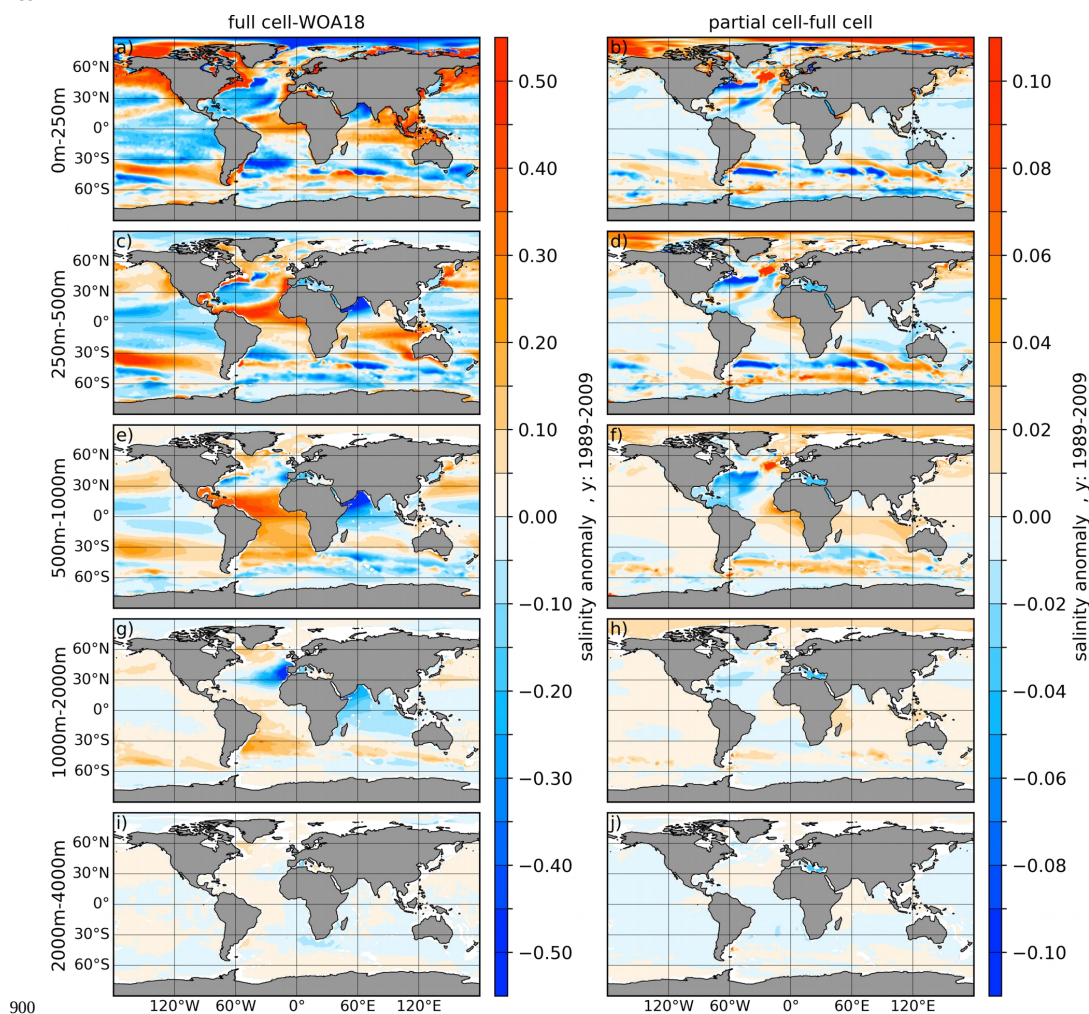
51



893 **Figure 1:** (Left column) Temperature biases full cells referenced to the World Ocean Atlas 2018 (WOA18,
894 Zweng et. al 2018) averaged over the period 1989-2009. The right column shows the temperature difference
896 between partial and full cells (partial minus full). From top to bottom the panels show the vertically averaged
897 fields for the depth ranges of 0-250 m, 250-500 m, 500-1000 m, 1000-2000 m and 2000-4000 m.
898
899



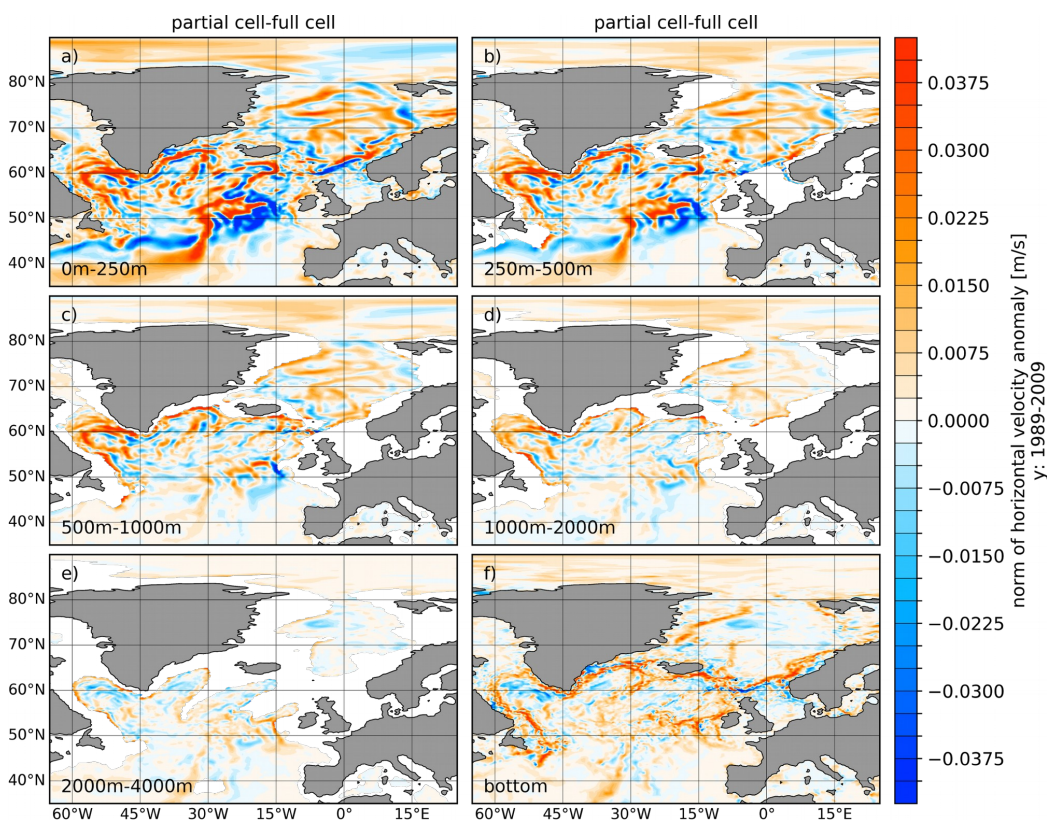
53



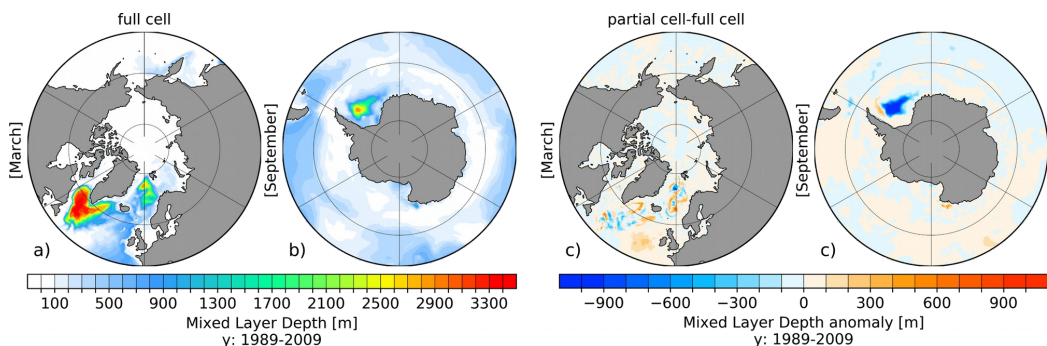
900
901 **Figure 2:** Same as Fig. 1, but for salinity.



55



902 **Figure 3:** Difference of the horizontal velocity norm between simulations with partial and full cells (partial-
 903 full) averaged over the period 1989-2009 and averaged over the depth ranges of 0-250 m, 250-500 m, 500-
 904 1000 m, 1000-2000 m and 2000-4000 m as well as the bottom value.
 905
 906
 907



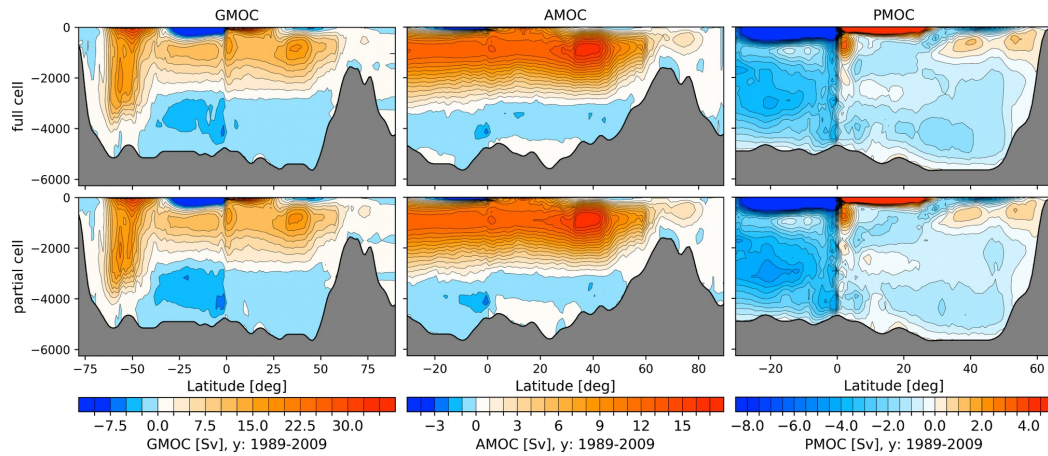
908 **Figure 4:** Northern hemispheric March (a) and southern Hemispheric September (b) mixed layer depth
 909 (MLD) with full cells as well as corresponding anomalous MLD with partial minus full cells (c, d), averaged
 910 for the period 1989-2009.
 911

56

28



57



912

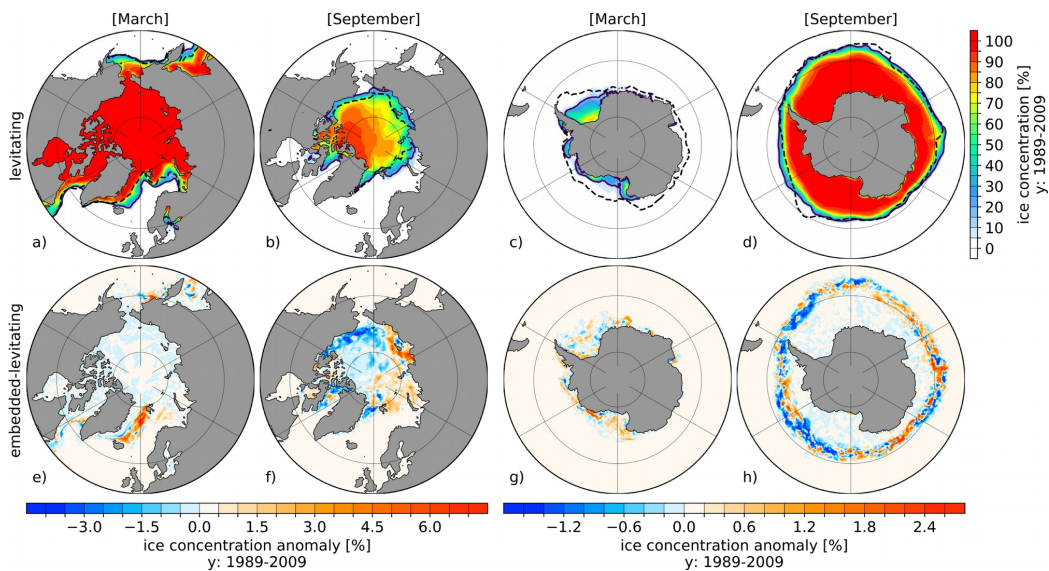
913 **Figure 5:** Global (GMOC, left column), Atlantic (AMOC, middle column) and Indo-Pacific (PMOC, right
914 column) Meridional Overturning Circulation for full cell (upper row) and partial cell (lower row) averaged
915 for the time period 1989-2009.

916

917



59



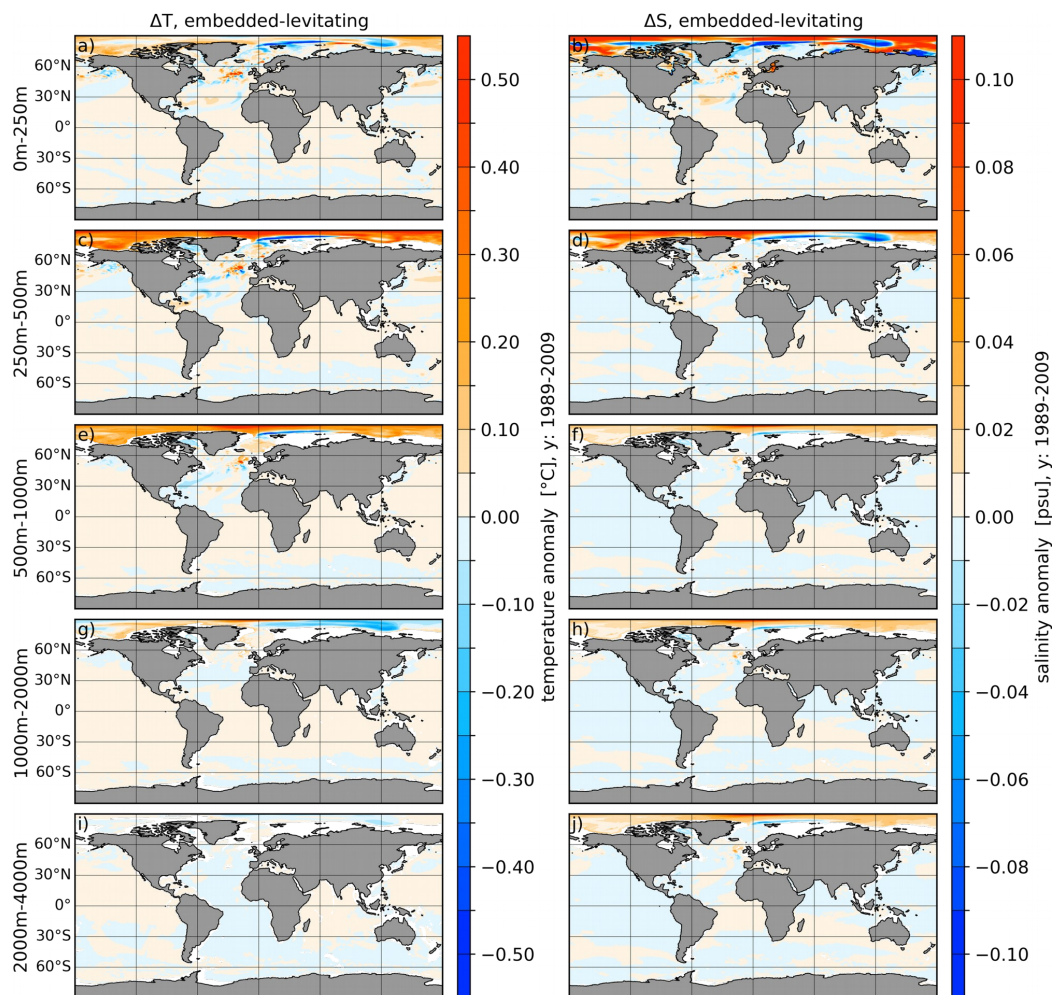
918

919 **Figure 6:** Levitating (upper row) northern and southern hemispheric March (a, c) and September (b, d) sea
920 ice concentration averaged for the period 1989-2009. Solid and dashed lines indicate the simulated and
921 observed (Cavalieri et al., 1996) contour of the 15% sea ice extent. The lower row shows the corresponding
922 sea ice concentration anomalies between embedded and levitating sea ice (embedded minus levitating)
923 averaged over the same period.

924



61



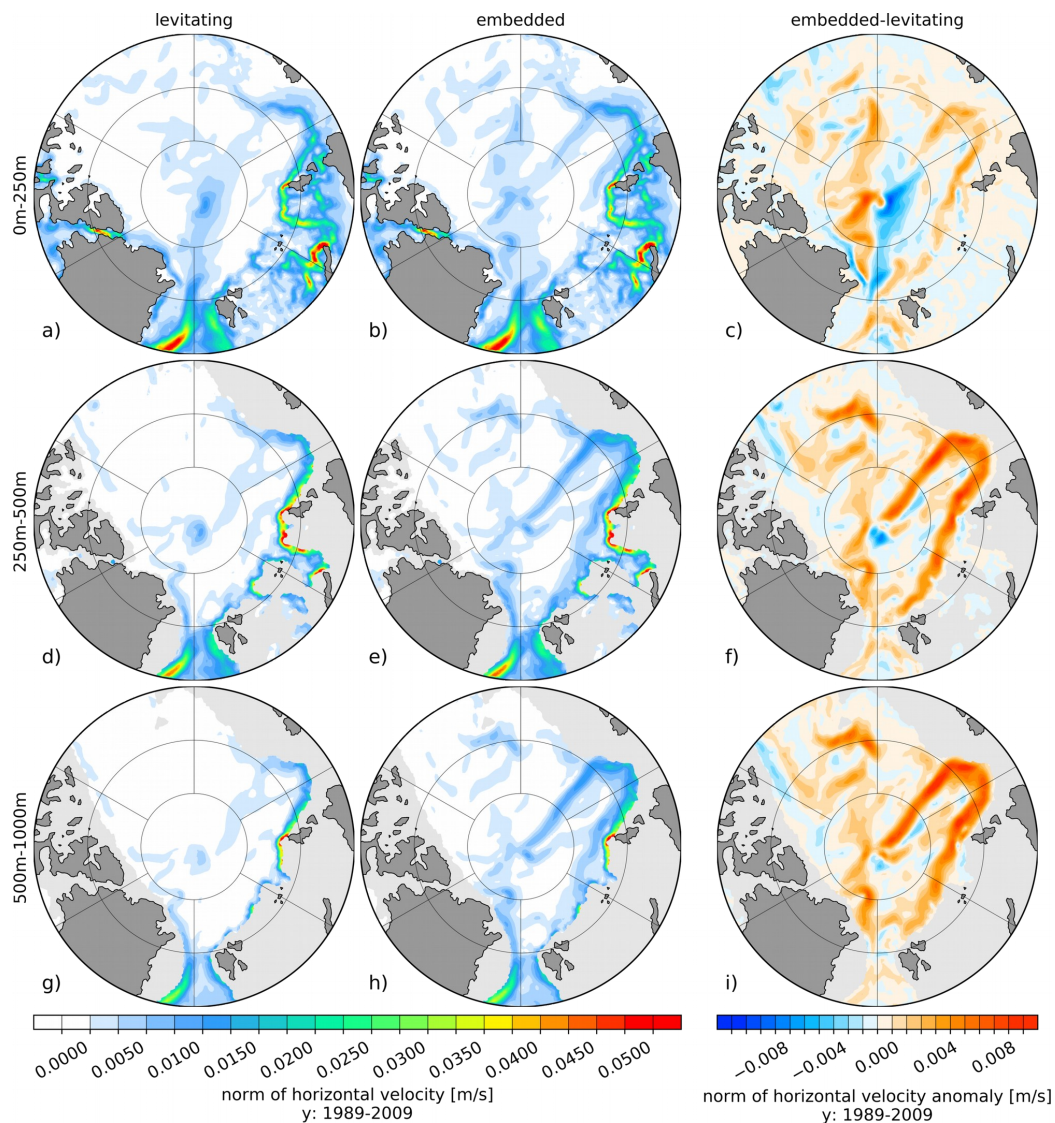
925

926 **Figure 7:** Temperature (left column) and salinity (right column) difference between embedded- and
927 levitating sea ice averaged for the period 1989 to 2009. From top to bottom, panels show the vertically
928 averaged fields for the depth ranges of 0-250 m, 250-500 m, 500-1000 m, 1000-2000 m and 2000-4000 m.

929



63



930

931 **Figure 8:** Norm of ocean velocity for levitating (left column) and floating (middle column) and the
 932 difference between embedded and levitating (right column) sea ice averaged for the period 1989 to 2009.
 933 From top to bottom, the panels show the vertically averaged fields for the depth ranges of 0-250 m, 250-500
 934 m and 500-1000 m.

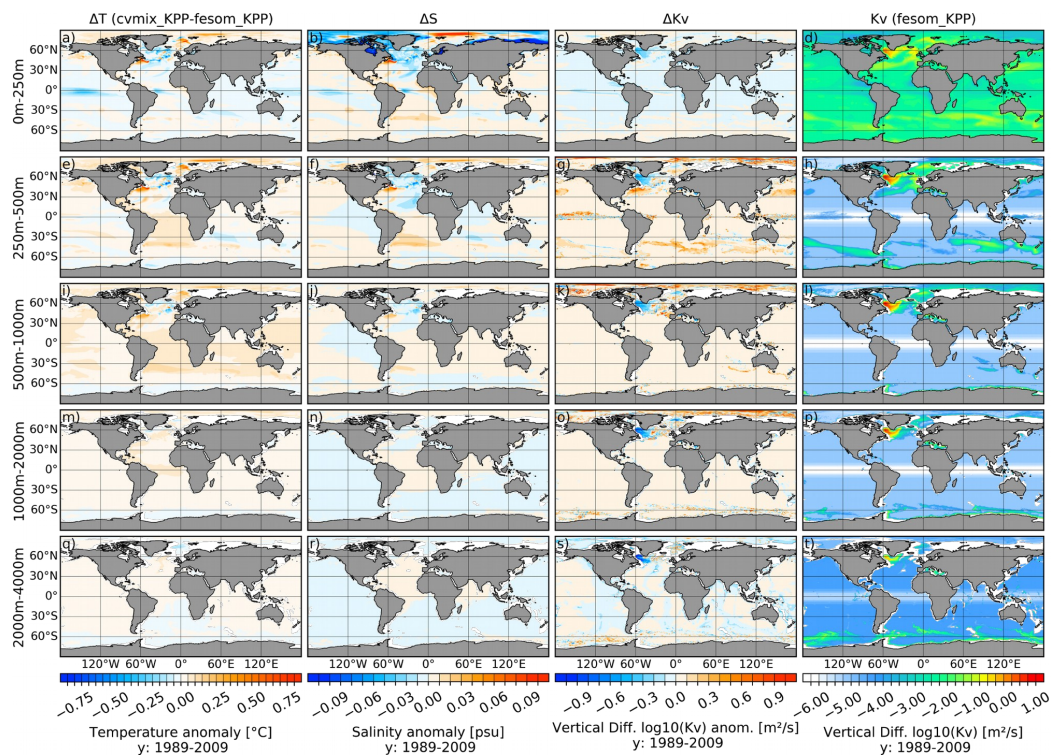
935

936

937



65

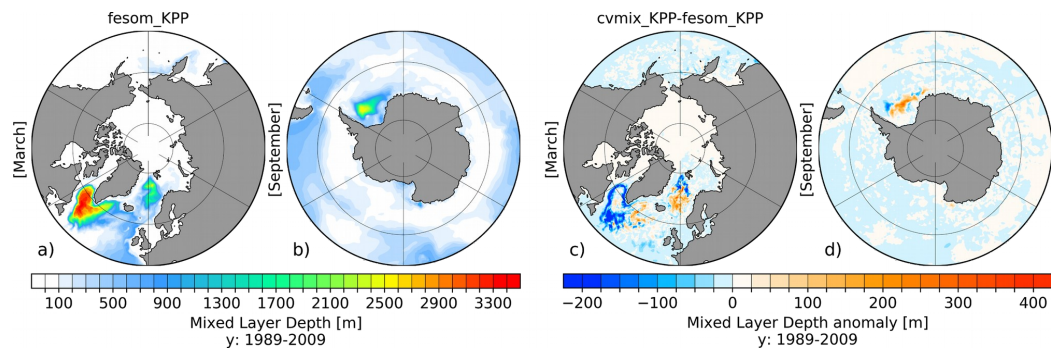


938

939 **Figure 9:** Temperature (1st Column), salinity (2nd column) and vertical diffusivity (3rd column) difference
 940 between cvmix_KPP and original fesom_KPP implementation as well as the absolute vertical diffusivity
 941 values (4th column) for fesom_KPP averaged for the period 1989 to 2009. From top to bottom, panels show
 942 the vertically averaged fields for the depth ranges of 0-250 m, 250-500 m, 500-1000 m, 1000-2000 m and
 943 2000-4000 m.

944

945

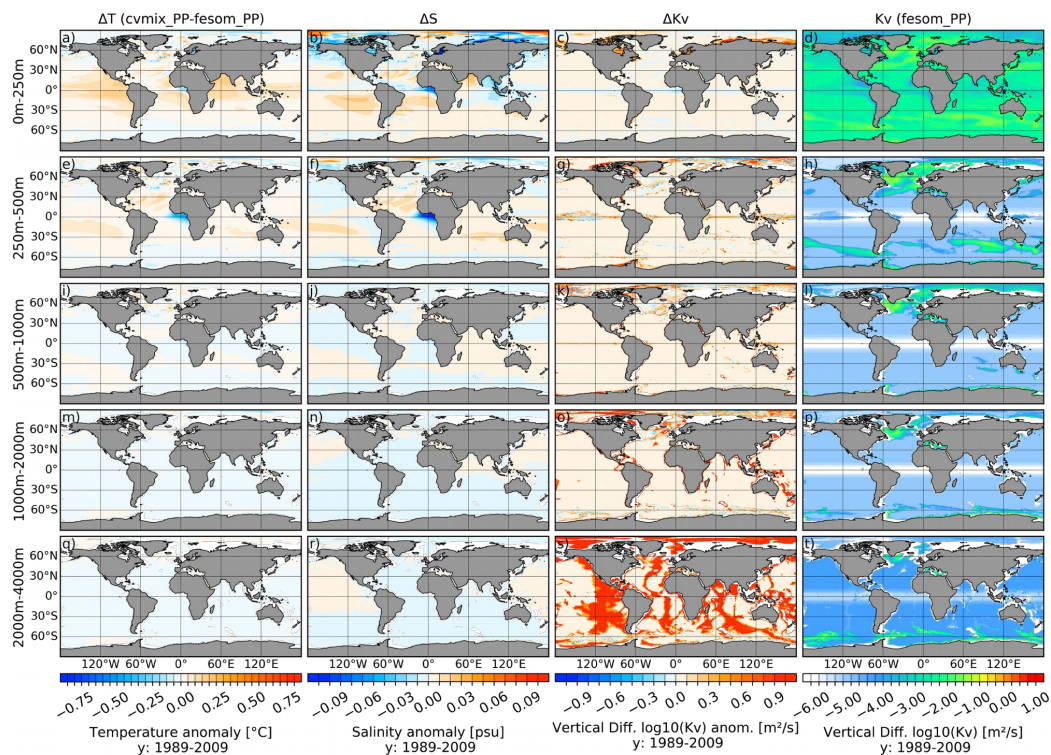


946

947 **Figure 10:** Northern hemispheric March (a) and southern Hemispheric September (b) mixed layer depth
 948 (MLD) for original FESOM2.0 KPP implementation as well as corresponding anomalous MLD between
 949 CVMIX and original FESOM2.0 KPP implementation (c, d), averaged for the period 1989-2009.



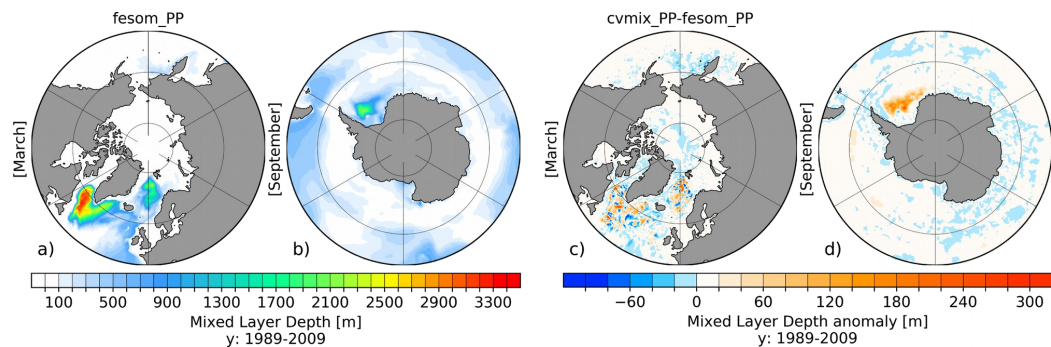
67



950

951 **Figure 11:** Temperature (1st Column), salinity (2nd column) and vertical diffusivity (3rd column) difference
 952 between cvmix_PP and original fesom_PP implementation as well as the absolute vertical diffusivity values
 953 (4th column) for fesom_PP averaged for the period 1989 to 2009. From top to bottom, panels show the
 954 vertically averaged fields for the depth ranges of 0-250 m, 250-500 m, 500-1000 m, 1000-2000 m and
 955 2000-4000 m.

956



957

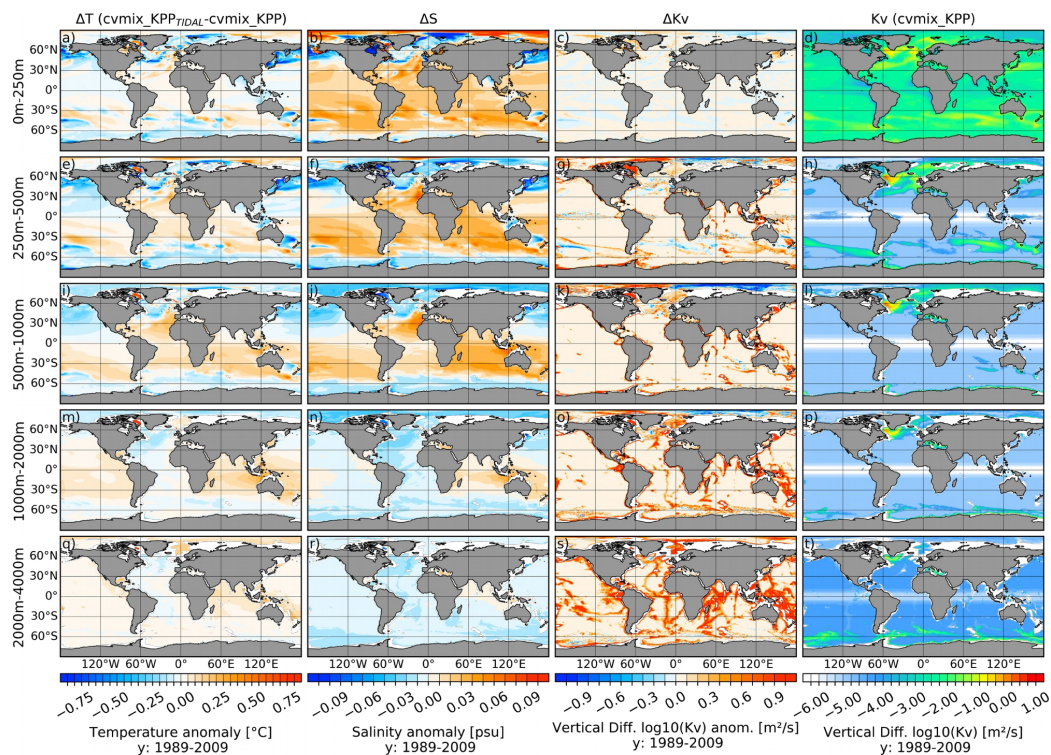
958 **Figure 12:** Northern hemispheric March (a) and southern Hemispheric September (b) mixed layer depth
 959 (MLD) for original FESOM2.0 PP implementation as well as corresponding anomalous MLD between
 960 CVMIX and original FESOM2.0 PP implementation (c, d), averaged for the period 1989-2009.

68

34



69



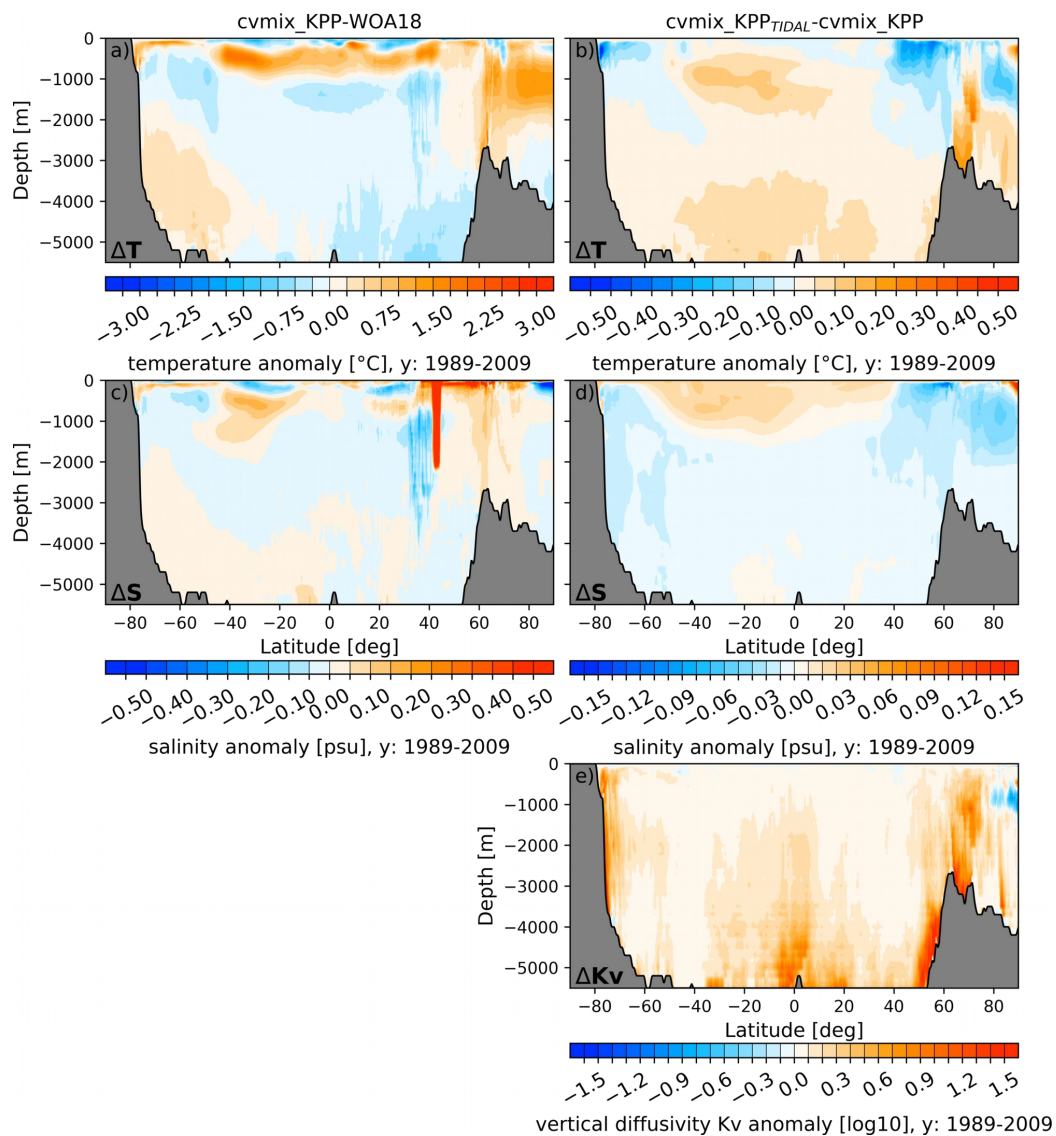
961

962 **Figure 13:** Temperature (1st Column), salinity (2nd column) and vertical diffusivity (3rd column) difference
 963 between CVMIX KPP with and without TIDAL mixing of Simmons et al. (2004) as well as the absolute
 964 vertical diffusivity values (4th column) for CVMIX KPP without TIDAL mixing averaged for the period
 965 1989 to 2009. From top to bottom, panels show the vertically averaged fields for the depth ranges of 0-250
 966 m, 250-500 m, 500-1000 m, 1000-2000 m and 2000-4000 m.

967



71



968

969 **Figure 14:** Global zonal averaged biases of temperature (a, b), salinity (c, d) and vertical diffusivity (e)
970 profiles of cvmix_KPP with respect to WOA18 (a, c) and of cvmix_KPP with tidal mixing of Simmons et al.
971 (2004) versus without (c, d, e).

972

973

974

975

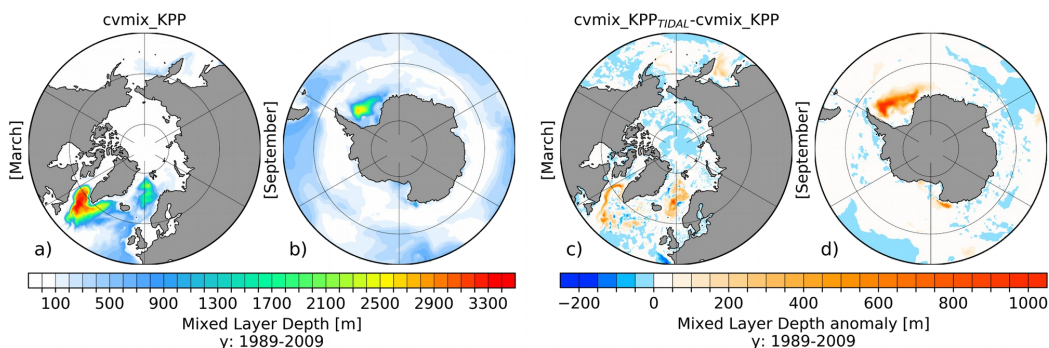
976

72

36



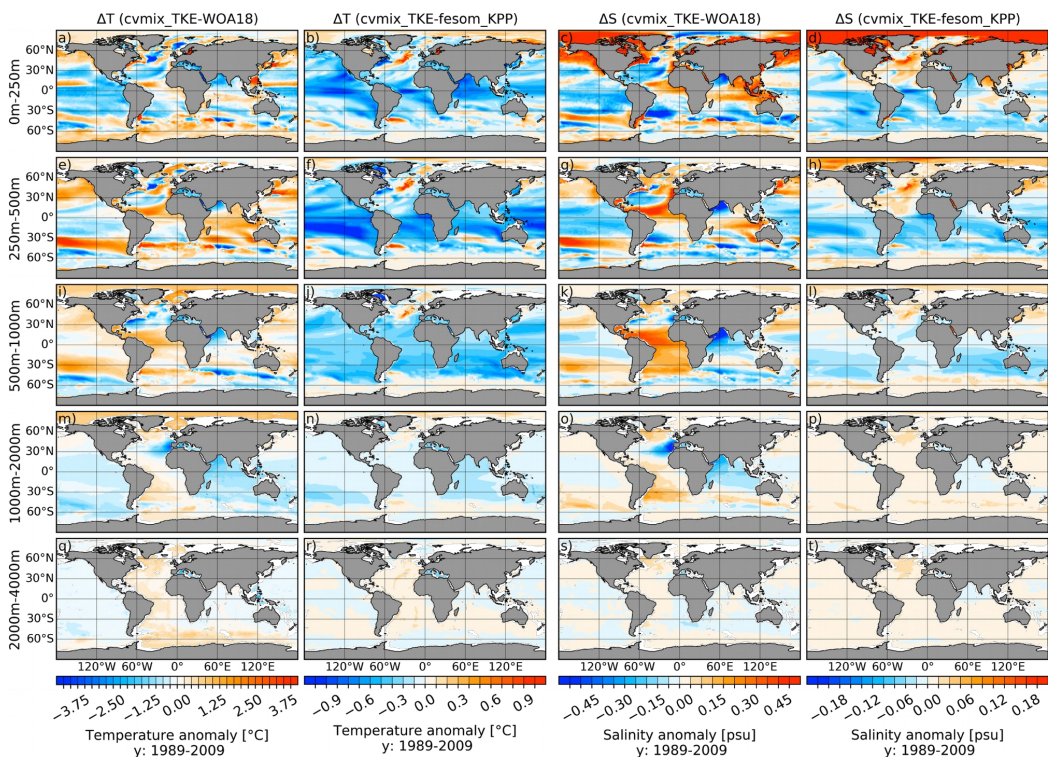
73



977

978 **Figure 15:** Northern hemispheric March (a) and southern Hemispheric September (b) mixed layer depth
 979 (MLD) for cvmix_KPP without TIDAL mixing as well as corresponding anomalous MLD between
 980 cvmix_KPP with minus without TIDAL mixing of Simmons et al. (2004)(c, d), averaged for the period
 981 1989-2009.

982



983

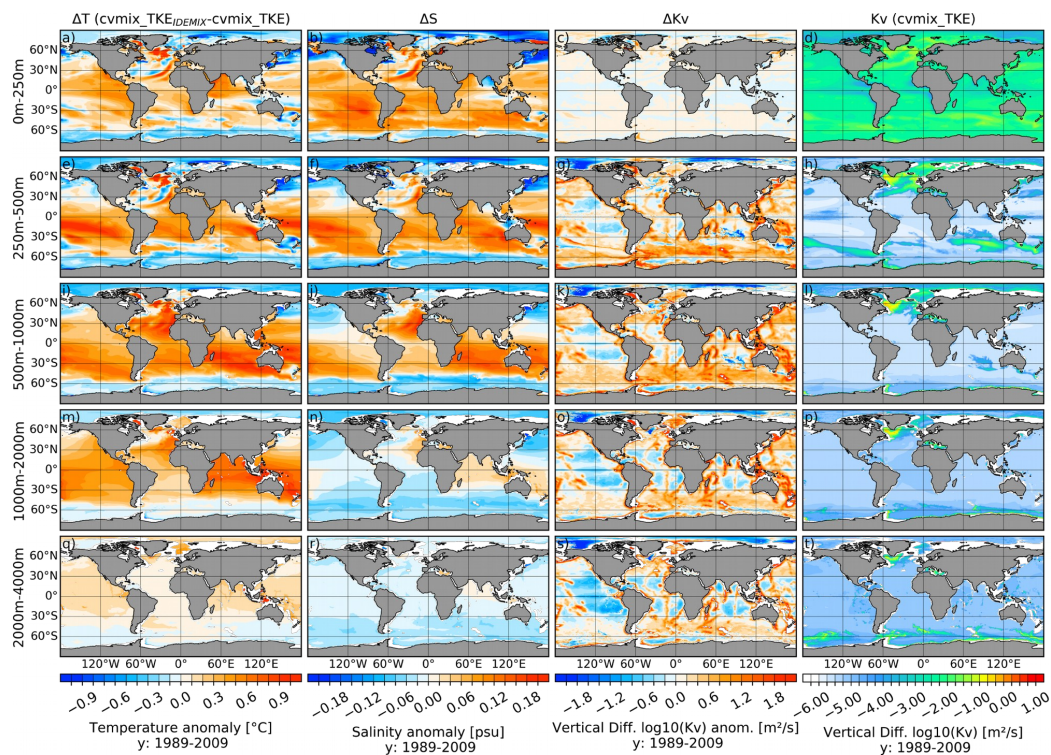
984 **Figure 16:** Temperature (1st and 2nd column), salinity (3rd and 4th column) difference between cvmix_TKE
 985 and WOA18 (1st and 3rd column) as well as between cvmix_TKE and fesom_KPP (2nd and 4th column)
 986 averaged for the period 1989 to 2009. From top to bottom, panels show the vertically averaged fields for the
 987 depth ranges of 0-250 m, 250-500 m, 500-1000 m, 1000-2000 m and 2000-4000 m.
 988

74

37



75



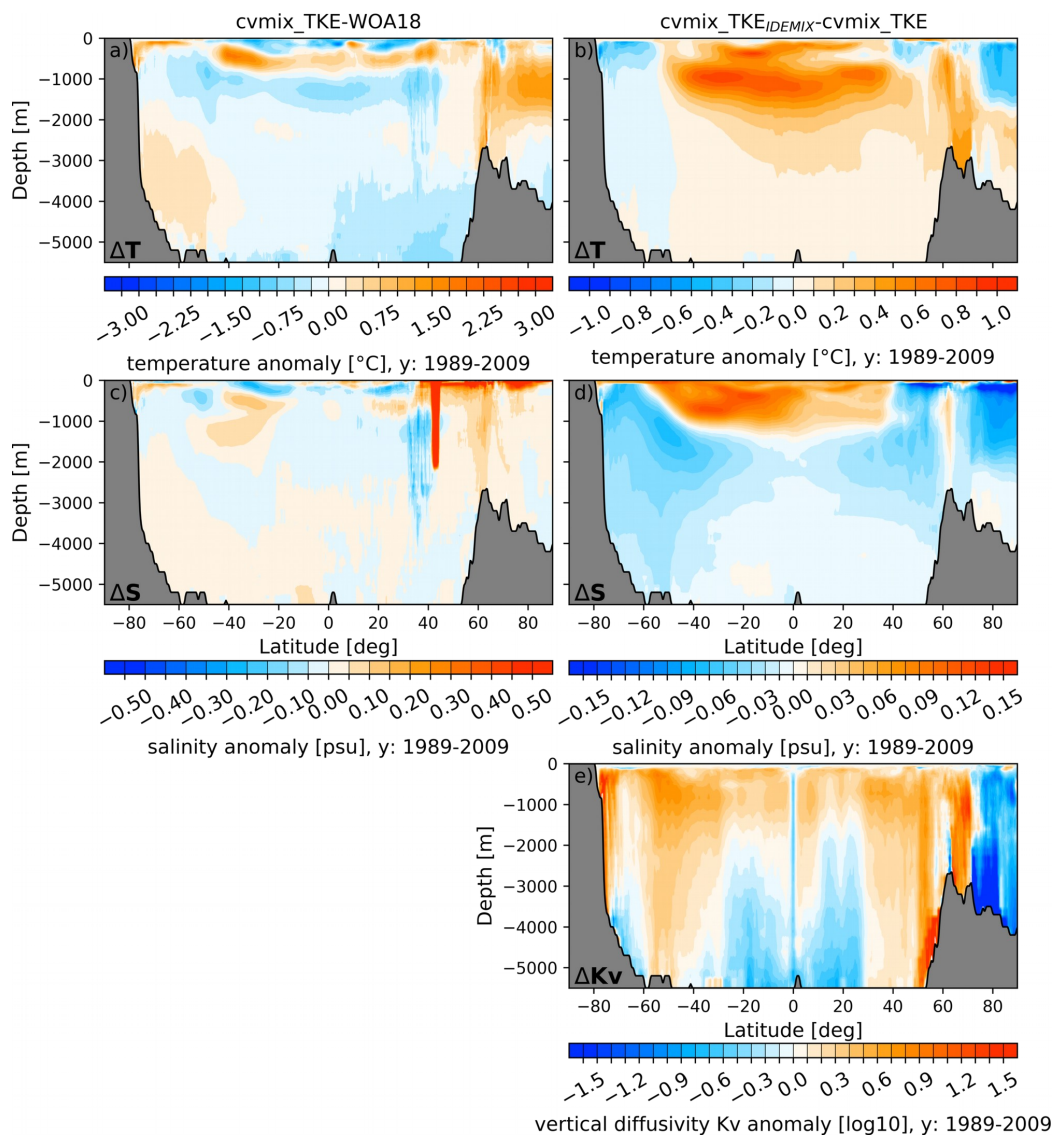
989

Figure 17: Temperature (1st Column), salinity (2nd column) and vertical diffusivity (3rd column) difference between cvmix_TKE with and without IDEMIX as well as the absolute vertical diffusivity values (4th column) for cvmix_TKE without IDEMIX mixing averaged for the period 1989 to 2009. From top to bottom, panels show the vertically averaged fields for the depth ranges of 0-250 m, 250-500 m, 500-1000 m, 1000-2000 m and 2000-4000 m.

995



77



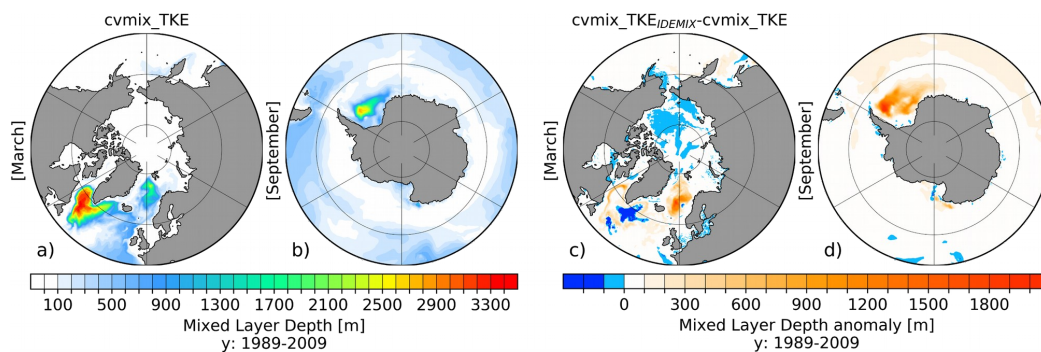
996

997 **Figure 18:** Global zonal averaged biases of temperature (a, b), salinity (c, d) and vertical diffusivity (e)
 998 profiles of cvmix_TKE with respect to WOA18 (a, c) and of cvmix_TKE with IDEMIX versus without (c, d,
 999 e).

1000



79



1001

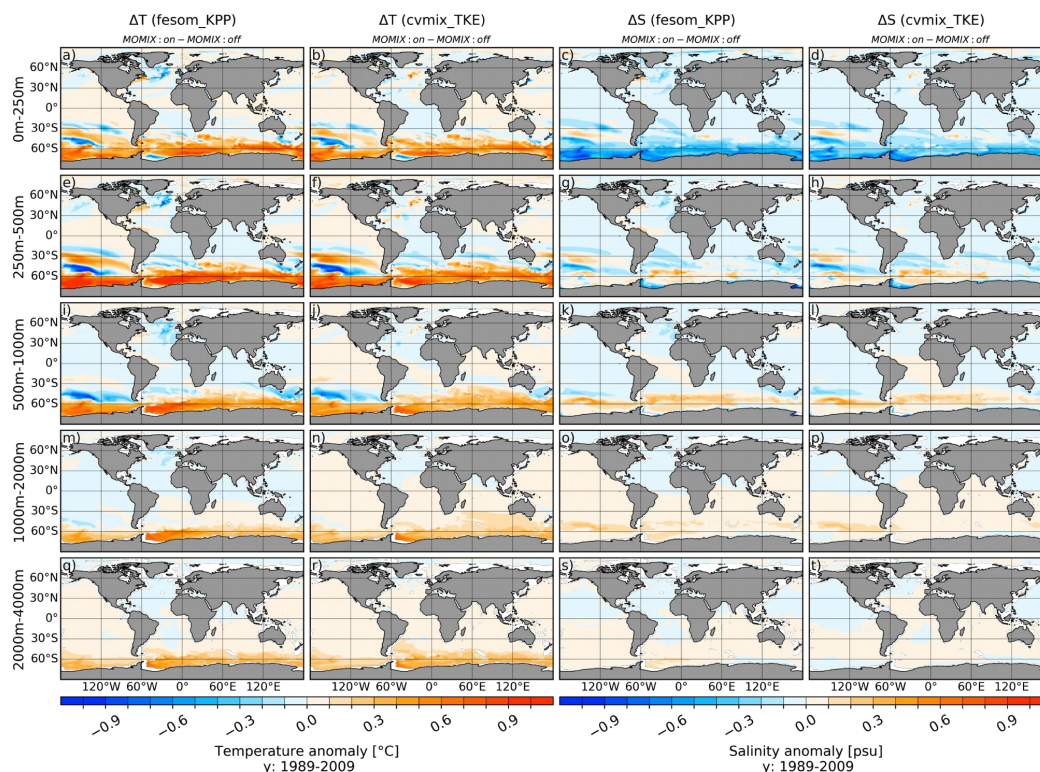
1002 **Figure 19:** Northern hemispheric March (a) and southern Hemispheric September (b) mixed layer depth
1003 (MLD) for cvmix_TKE without IDEMIX mixing as well as corresponding anomalous MLD between
1004 cvmix_TKE with minus without IDEMIX mixing, averaged for the period 1989-2009.

1005

1006

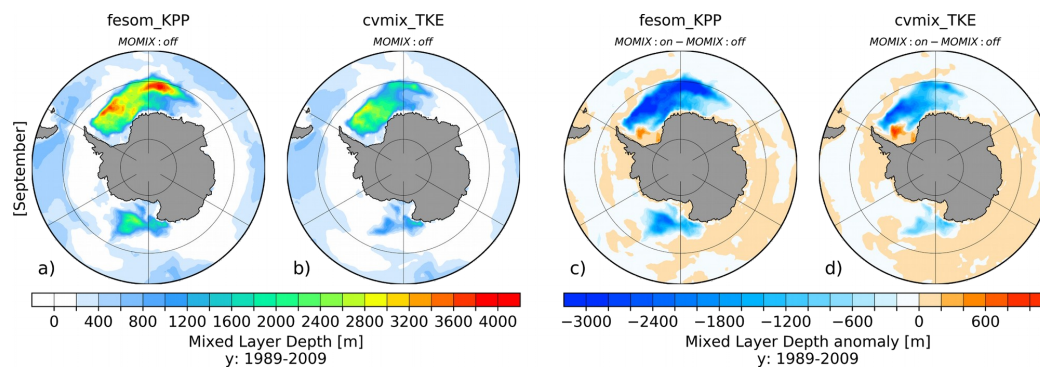


81



1007
 1008 **Figure 20:** Temperature (1st and 2nd column), salinity (3rd and 4th column) difference between fesom_KPP
 1009 and cvmix_TKE vertical mixing parameterisation with Monin-Obukov vertical mixing (MOMIX) switch on
 1010 and off (MOMIX: on minus MOMIX: off) averaged for the period 1989 to 2009. From top to bottom, panels
 1011 show the vertically averaged fields for the depth ranges of 0-250 m, 250-500 m, 500-1000 m, 1000-2000 m
 1012 and 2000-4000 m.

1013



1014
 1015 **Figure 21:** Southern Hemispheric September mixed layer depth (MLD) for fesom_KPP (a) and cvmix_TKE
 1016 (b) with switch off Monin-Obukov vertical mixing (MOMIX) parameterisation as well as corresponding
 1017 anomalous MLD between switched on and off MOMIX parameterisation (c, d, MOMIX: on minus MOMIX:
 1018 off), averaged for the period 1989-2009.

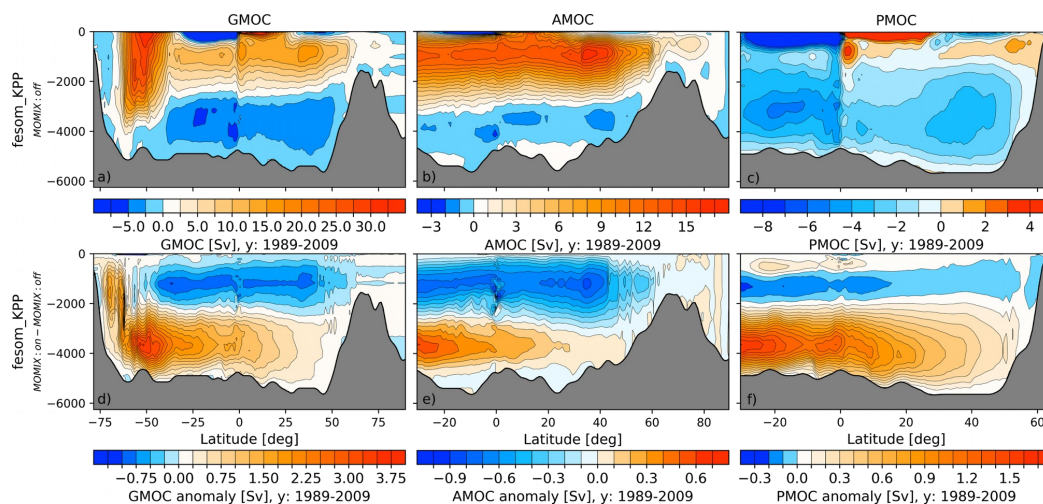
1019

82

41



83
1020



1021
1022 **Figure 22:** Absolute (upper row) and anomalous (lower row) Global (GMOC, left column), Atlantic
1023 (AMOC, middle column) and Indo-Pacific (PMOC, right column) Meridional Overturning Circulation,
1024 averaged for the time period 1989-2009. Absolute values are shown for fesom_KPP with switched off
1025 Monin-Obukov vertical mixing (MOMIX) parameterisation, anomalous values show the difference between
1026 fesom_KPP with switch on/off MOMIX parameterisation MOMIX: on minus MOMIX: off.

1027